strain
An International Journal for Experimental Mechanics

Identification of Johnson–Cook's Viscoplastic Model Parameters Using the Virtual Fields Method: Application to Titanium Alloy Ti6Al4V

D. Notta-Cuvier*†‡, B. Langrand*, E. Markiewicz†‡, F.Lauro†‡ and G. Portemont*

*Onera – The French Aerospace Lab, F-59045, Lille, France

†Université Lille Nord de France, F-59000 Lille, France

‡Université de Valenciennes (UVHC), LAMIH/CNRS-FRE 3304, F-59313 Valenciennes, France

ABSTRACT: The identification of viscoplastic material parameters is addressed using a new powerful method: the virtual fields method (VFM). Contrary to classical procedures that are statically determined, the VFM is applied to heterogeneous mechanical fields. Without any hypotheses of homogeneity required, the exploitation of tests with the VFM is not limited to small levels of strains anymore and it can be taken advantage of the large amount of information available thanks to full-field measurements. In the case of viscoplastic models, the characterisation of strain-rate sensitivity with the VFM is attempted in this paper using only one test under high-speed loading conditions, whereas several tests performed at different constant strain-rates are required for the classical procedures. This article focuses on the development of the VFM for the characterisation of Johnson–Cook's (JC) viscoplastic model. To his aim a return-mapping algorithm was developed according to the JC's model with an implicit Euler scheme implemented to integrate the constitutive relations. The whole viscoplastic behaviour of a Titanium alloy (Ti6Al4V) is successfully characterised by the VFM using only two tensile tests on notched flat specimens, with full-field strain measurements by digital image correlation.

KEY WORDS: *digital image correlation, Johnson–Cook, Titanium alloy, virtual fields method, viscoplasticity*

Introduction

The characterisation of mechanical material behaviour under high rate loadings remains a challenge, particularly when the number of material parameters governing the constitutive equations is significant. This is the case when considering anisotropic materials and/or strongly nonlinear constitutive laws, for example, in viscoplasticity or damage theories. The classical procedures of identification of material parameters require to perform several normalised tests (e.g. tensile tests) to fit the model with experimental data. The exploitation of these tests is usually statically determined, i.e. it assumes that the mechanical fields (in particular strain and strain-rate) are homogeneous over the specimen's region of interest. Yet, such a hypothesis is obviously violated as soon as plastic localisation (e.g. necking) occurs in the material [1]. In the case of many polymers, for example, the early presence of necking makes the determination of uniaxial true stress-strain curve impossible from a classical tensile testing [2]. More generally, tests exploitation is anyway limited to small levels of strain, before localisation. Moreover, material parameters are determined with tests in one direction of loading. Consequently, a large number of tests are required when complex behaviours are involved. For example, several tests have to be performed at constant strain-rate to characterise the strain-rate sensitivity of a material.

These drawbacks can be avoided by dealing with heterogeneous kinematic fields, with no hypothesis on their nature anymore (i.e. statically undetermined approach). The measurement of heterogeneous mechanical fields provides very rich experimental data and allows to extract more information from a smaller number of tests. In particular, the heterogeneity of strain-rate can lead to a sufficient involvement of viscoplastic material parameters in the specimen response to attempt their identification in a reduced number of tests.

The development of full-field measurement techniques now gives easy access to heterogeneous mechanical fields. These techniques, such as digital image correlation (DIC) [3–5], moiré [6, 7] and speckle interferometry [8] and grid methods [9–11], provide a very large amount of experimental data (about 1000–10000 points of measurement). In addition, full-field techniques allow to focus on specific areas of measurement (e.g. zones of strain localisation), which may be used to improve the accuracy of the identification.

An overview of procedures developed to identify material parameters from full-field measurements was established by Avril *et al.* [12]. The most widespread approach is the Finite Element Model Updating (FEMU) method. Iterative finite element (FE) simulations are processed until constitutive parameters leading to the best match between FE computations and experimental measurements are found. Generally, FEMU method considers the discrepancy between known and predicted quantities (e.g. loads for FEMU-F methods [13]) or displacement fields for FEMU-U methods [13, 14]. All FEMU methods are sensitive to mesh discretisation and modelling errors. In particular, boundary conditions have to be perfectly known and modelled. Meuwissen *et al.* [15] are the pioneers in the application of FEMU method to elastoplastic behaviours. Markiewicz *et al.* [16] extended this approach to elasto-viscoplasticity, using the Cowper-Symonds model [17], and more recently, Kajberg *et al.* [18] to Perzyna [19] model and Kajberg and Wikman [20] to Johnson and Cook [21] model.

Note that many FEMU methods (FEMU-F methods in particular) do not require field measurements. On the

doi: 10.1111/str.12010

contrary, other approaches are dedicated to their treatment. For example, Coppieters *et al.* [22] identified material parameters by minimising the discrepancy between the internal and external works that are computed using full-field measurements of strains. Some other methods are presented by Avril *et al.* [12]: the Equilibrium Gap Method (EGM) [23] or the Reciprocity Gap Method (RGM) [24], for example, The RGM needs strain field measurements over the boundary and the EGM needs strain field measurements over the whole domain of interest. Both RGM and EGM can be actually considered as particular applications of an other method of identification: the virtual fields method (VFM), respectively, when kinematic fields are known only on the boundary or for some piecewise particular fields.

The VFM, introduced by Grédiac [25], is dedicated to the treatment of full-field strain measurements. It is based on the principle of virtual work (PVW) that expresses the global equilibrium of a solid of any shape. One of the main advantages of the VFM compared to FEMU methods is that it does not require to build a numerical model of the material test. Provided convenient virtual displacement fields, the VFM can be carried out knowing only the resultant of applied loads. In addition, the characterisation with the VFM of linear constitutive laws is based on the resolution of a linear system of equations and is consequently no time-consuming, whereas FEMU methods always require costly iterative computations of FE models. In the case of linear elasticity, for example, the identification by the VFM of in-plane [26] and bending [27, 28] rigidities of anisotropic materials is proven to be accurate and robust. A drawback is that it may be quite difficult and tedious to find out as many suitable virtual fields as number of parameters to be identified when the latter is important. Yet, improvements proposed by Grédiac *et al.* [29] allow to build suitable special virtual fields following a systematic procedure. In addition, the use of these special virtual fields is proven to improve the accuracy and the robustness of the VFM for the characterisation of linear constitutive laws [30, 31]. In particular, the sensitivity of results to noisy data can be greatly decreased [32]. An other interesting approach consists in building piecewise virtual fields [33].

For nonlinear constitutive equations (e.g. plasticity, viscoplasticity, damage), there is generally no explicit relation between stress components and measured strain fields involving unknown material parameters. Consequently, their identification with the VFM is based on an iterative procedure of minimisation of equilibrium gaps to respect the PVW. In this case, numerical tools are needed to compute mechanical fields (in particular stress components) from measured strain fields to express the virtual works. Some studies [34–36] have demonstrated that linear isotropic hardening laws (J_2-plasticity) can be characterised with the VFM, using simple virtual fields. Other studies tried to improve the method by defining optimised virtual fields [37] similarly to special virtual fields used in the case of linear constitutive laws. Optimised virtual fields were used to characterise a more complex elastoplastic model taking into account kinematic hardening. Recently, Rossi and Pierron [38] have extended the formulation of the method to large displacements and have demonstrated the ability of the VFM to characterise elastoplastic models of behaviour using numerically simulated 3-dimensional fields.

All these applications consider quasi-static loading conditions. Giraudeau and Pierron [39] and Giraudeau *et al.* [40] proved that the VFM can be used in the particular dynamic framework of vibrating plates, as an alternative to modal analysis, to identify stiffness and damping parameters (pure harmonic bending, linear behaviour). Indeed, in these cases, the virtual work of acceleration can be simply computed thanks to the knowledge of the imposed sinusoidal excitations. Moulart *et al.* [41] and Pierron and Forquin [42] used the VFM to identify the stiffnesses (linear orthotropic elasticity) of a composite and the Young's modulus (unidimensional behaviour) of a concrete material, respectively, with dynamic tests taking into account inertia effects. To the authors' knowledge, only Avril *et al.* [43] have studied the characterisation of a viscoplastic model of behaviour using the VFM, processing data of a dynamic test without inertia effects. In this article, the PVW was rewritten in a rate-dependent form to identify the hardening parameters and the strain-rate sensitivity exponent of Perzyna's model. Stress components were computed using an Euler scheme between two instants of strain field measurement. Experimental results showed a quite precise identification of the quasi-static initial yield stress. Nevertheless, high differences between expected and identified values of hardening parameters and strain-rate sensitivity exponent were found. Note that these differences were mainly due to a lack of uniqueness of the solution (test was not rich enough). Consequently, the potential of the VFM could not be totally investigated.

The ability of the VFM to characterise the whole viscoplastic model of Johnson and Cook [21] was demonstrated by the authors from numerically simulated strain fields [44]. Mechanical quantities (stresses, cumulated plastic-strain, strain-rate …) were computed from strain fields by return-mapping algorithms, according to Johnson–Cook's constitutive laws. Tests demonstrated the ability of the VFM to deal with the strongly nonlinear plastic part (i.e. rate independent) of the model. Then, FE simulations (using the explicit FE code Europlexus) in dynamic conditions proved the possibility to characterise a strain-rate sensitivity with the VFM.

In this article, the experimental identification of the whole set of parameters of Johnson–Cook's viscoplastic model is attempted using the VFM and full-fields strain measurements, by DIC. To this aim, a return-mapping algorithm was developed according to the JC's viscoplastic model with an implicit Euler scheme implemented to integrate the constitutive relations. The material tested is a Titanium alloy Ti6Al4V. Ti6Al4V is the most widespread Titanium alloy (more than 50% of sales in mass) with about 80% of the production designed for aeronautical applications (e.g. turbine of reactors). Numerous studies [45–47] showed that the constitutive laws of the Johnson–Cook (JC) model [21] are suitable to describe the strongly strain-

doi: 10.1111/str.12010

rate-dependent behaviour of Ti6Al4V. A particularity of JC's model is to isolate the effects of strain, strain-rate and temperature on the hardening/softening of the material (cf. Johnson–Cook's Viscoplastic Behaviour Model section). It leads to classical procedures of characterisation of JC's model divided into two steps (assuming there is no effect of temperature): material parameters governing strain hardening and viscoplastic parameters governing strain-rate sensitivity are successively identified. The VFM, presented in detail in The Virtual Fields Method section, is applied in this way to identify JC's material parameters for Ti6Al4V. First, notched flat specimens are subjected to quasi-static tensile tests to characterise the plastic part (i.e. rate-independent) of the model (cf. Characterisation of the plastic part of the model section). As mentioned before, the VFM (statically undetermined approach) is able to deal with the strongly heterogeneous mechanical fields that are here generated on the specimen thanks to the presence of the notches. The heterogeneity of strain-rate fields provides a rich information about the strain-rate sensitivity of the material. Therefore, the characterisation of the viscoplastic part of JC's model with the VFM is attempted using a single dynamic tensile test (cf. Characterisation of the strain-rate sensitivity of Ti6Al4V section), whereas several statically determined tests, at constant strain-rate, are required when using classical procedures. The JC's model characterised for Ti6Al4V by the VFM from these only two tests is discussed in Relevance of the JC's model characterised with the VFM section.

Johnson–Cook's Viscoplastic Behaviour Model

The general framework of viscoplastic theory for metallic materials assumes the partition of the total strain tensor, $\bar{\bar{\varepsilon}}$, into a reversible (elastic) part, $\bar{\bar{\varepsilon}}^e$, and an irreversible one. Here, the latter is considered as a viscoplastic part, $\bar{\bar{\varepsilon}}^{vp}$, and $\bar{\bar{\varepsilon}} = \bar{\bar{\varepsilon}}^e + \bar{\bar{\varepsilon}}^{vp}$. The von Mises criterion for plasticity (or J_2 criterion) is used. It gives rise to the expression (1) for the yield surface in stress space, with σ_y the current yield stress.

$$f = J_2(\bar{\bar{\sigma}} - \bar{\bar{\beta}}) - \sigma_y \tag{1}$$

with $\bar{\bar{\sigma}}$ the Cauchy stress tensor and $\bar{\bar{\beta}}$ the kinematic hardening variable, or 'back-stress'. $J_2(\bar{\bar{x}}) = \sqrt{\frac{3}{2}\mathrm{dev}(\bar{\bar{x}}) : \mathrm{dev}(\bar{\bar{x}})}$, with $\mathrm{dev}(\bar{\bar{x}})$ the deviatoric part of tensor $\bar{\bar{x}}$. Without kinematic hardening, $J_2(\bar{\bar{\sigma}})$ is the von Mises equivalent stress.

Elastic stress states are characterised by $f < 0$. Plastic or viscoplastic flow occurs as soon as $f = 0$. Then, the yield surface evolves following the hardening laws that allows to compute the current yield stress, σ_y, and 'back-stress', $\bar{\bar{\beta}}$.

Numerous empirical and semi-empirical models have been proposed to describe plastic and viscoplastic material behaviours [48]. Among them, the Johnson–Cook (JC) model, proposed in the early 1980s [21], is one of the most widely used for industrial applications. Indeed, it generally describes very well the behaviour of metallic materials submitted to high strains, strain-rates and temperatures [46, 47, 49], although it is a purely empirical (i.e. phenomenological) model. Moreover, the model is numerically robust, that makes attractive its implementation within a FE code, and can be easily calibrated thanks to the isolation of effects of strain, strain-rate and temperature on the hardening/softening's law (2) of the material. Strain hardening is isotropic and modelled by a power law of cumulated viscoplastic strain, p, defined by Equation (3), with parameters σ_0, the initial yield stress, and K and n, the isotropic hardening modulus and exponent, respectively. Viscous effects are taken into account as soon as the equivalent viscoplastic strain-rate, $\dot{\varepsilon}_{eq}^{vp}$, becomes higher than the threshold $\dot{\varepsilon}_0$. Strain-rate sensitivity is then governed by the viscoplastic parameter, M. In the same way, thermal softening is modelled as soon as the temperature, T, becomes higher than a reference temperature, T_0. T_0, exponent m and T_m (melting temperature under ambient pressure) are material parameters. In this study, tests are performed at ambient and constant temperature. In addition, the heat generation due to plastic work is negligible for metallic materials for the strain-rate range (up to 300 s^{-1}, locally) considered in this paper [50]. Consequently, thermal softening is neglected and the expression (2) of the isotropic hardening law of Johnson–Cook's model is limited to the two first parentheses. No kinematic hardening is taken into account.

$$\sigma_y = (\sigma_0 + Kp^n)\left(1 + M\ln\left(\frac{\dot{\varepsilon}_{eq}^{vp}}{\dot{\varepsilon}_0}\right)\right)\left(1 - \left(\frac{T - T_0}{T_m - T_0}\right)^m\right) \tag{2}$$

$$p = \int_0^t \sqrt{\frac{2}{3}\dot{\bar{\bar{\varepsilon}}}^{vp} : \dot{\bar{\bar{\varepsilon}}}^{vp}}\,\mathrm{d}t \tag{3}$$

As presented in Introduction section, the classical procedure for characterisation of viscoplastic models requires to perform several statically determined tests, for instance uni-axial tensile tests, each of them at constant strain-rate. Such a procedure was previously carried out to identify the material parameters of JC's model for Titanium alloy Ti6Al4V. Smooth cylindrical specimens (Figure 1) were

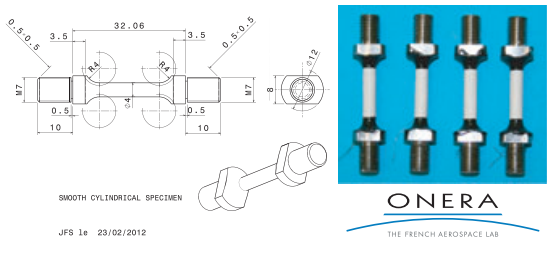

Figure 1: Classical procedure for viscoplastic behaviour characterisation: smooth cylindrical specimen geometry (dimensions in mm)

doi: 10.1111/str.12010

Table 1: Identified Johnson–Cook's parameters of Ti6Al4V – classic procedure

Material parameter	Identified value
Young modulus, E	114 GPa
Poisson coefficient, ν	0.342; Boyer *et al.* [60]
Initial yield stress, σ_0	973 MPa
Isotropic hardening modulus, K	557.3 MPa
Isotropic hardening exponent, n	0.5632
Equivalent strain-rate threshold, $\dot{\varepsilon}_0$	1.29 s^{-1}
Viscoplastic parameter, M	0.0329

subjected to uni-axial tensile tests. They were performed on a hydraulic jack, using a specific experimental device [51, 52]. Loading conditions were quasi-static (displacement rate of 2 mm min^{-1}, $\dot{\varepsilon}^p = 4.5\,10^{-3}\,s^{-1}$) and dynamic (displacement rates up to 6 m s^{-1}).

The force time history was measured by a piezoelectric load cell (Kistler 9071A; Kistler Instrumente AG, Winterthur, Switzerland). The time history of the relative displacement of the grips was measured by a laser transducer (Keyence LC2450; Keyence France SAS, Courbevoie, France) under quasi-static loading conditions and by an optical extensometer (Zimmer 200XH, Romulus, MI, USA) under dynamic loading conditions. Five tests were performed for each experimental configuration, with a quite low standard deviation. For example, the difference between the average ultimate stress and its minimum (or maximum) was <3%.

The exploitation of data is presented in detail in Appendix A. The values of JC's material parameters for the Ti6Al4V identified using this classical procedure are summarised in Table 1. The model built with these identified values matched well the mechanical behaviour of the material up to strain-rates about 500 s^{-1} and plastic strain about 5% (Figure 2). Indeed, the average gap between the model and the experiment was <2% and gaps exceed 5% for few data only. Nevertheless, it is likely that gaps would have been more important for higher levels of hardening. Obviously, the relevance of the results of identification would have been improved with the ability to exploit tests at higher strain ranges.

Although effective, this classical procedure of characterisation requires to perform several tests that have to be strongly normalised to ensure homogeneous strains and strain-rates. Carrying out these experiments is often challenging and costly. Moreover, as highlighted in Appendix A, the identification of viscoplastic parameters requires the user to make arbitrary choices, like the choice of a particular range for the strain rate threshold. Dealing with heterogeneous mechanical fields is an interesting alternative to overcome all these drawbacks. First, experiments are less constrained as no hypothesis of homogeneity, in particular for strain-rate fields, is required. In addition, the

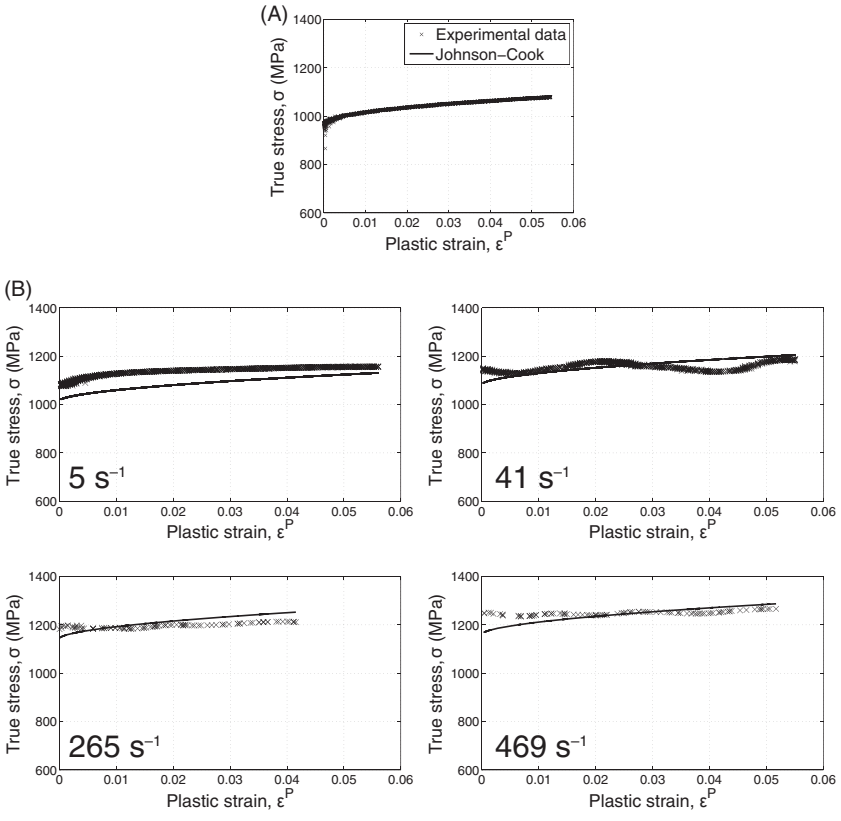

Figure 2: Johnson–Cook's (JC) model of behaviour of Ti6Al4V characterised with the classical procedure – (A) quasi-static loading conditions; (B) dynamic loading conditions (markers stand for experimental data, lines for the JC model)

doi: 10.1111/str.12010

measurement of heterogeneous mechanical fields allows to extract an enriched information from a smaller number of tests. In particular, the characterisation of the strain-rate sensitivity (in the strain-rate range characteristic of the heterogeneous strain-rate fields which are generated) becomes possible using only one tensile test under high-speed loading conditions. In this paper, the VFM is carried out for the characterisation of the whole viscoplastic behaviour of Ti6Al4V, using measurements of heterogeneous strain fields by DIC.

The Virtual Fields Method

The PVW (Equation 4) expresses the global equilibrium of a solid of volume V [53]. The several integrals stand for the virtual work of acceleration, volume external forces (body forces), surface external forces and internal forces, respectively. The PVW is verified for any kinematically admissible virtual displacement field $\vec{u}^*$, that is, $\vec{u}^*$ must be continuous and differentiable across the whole volume V.

$$\int_V \rho\vec{\gamma}.\vec{u}^* \mathrm{d}V = \int_V \vec{f}.\vec{u}^* \mathrm{d}V + \int_{S_f} \vec{T}.\vec{u}^* \mathrm{d}S - \int_V \bar{\sigma} : \bar{\varepsilon}^* \mathrm{d}V \tag{4}$$

where ρ is the material density, $\vec{\gamma}$ the acceleration field, $\vec{f}$ the body forces vector acting on V, $\vec{T}$ the stress vector acting on S_f. $\bar{\sigma}$ is the Cauchy stress tensor; $\bar{\varepsilon}^*$ is the virtual strain tensor derived from the kinematically admissible virtual displacement, $\vec{u}^*$, such that $\varepsilon^*_{ij} = \frac{1}{2}\left[\frac{\partial u^*_i}{\partial x_j} + \frac{\partial u^*_j}{\partial x_i}\right]$.

For the small masses of the tensile specimens used (about a few grams), body forces (i.e. here only weight) can be neglected and the external virtual work, w^*_{ext}, only takes surface forces applied on S_f into account. The acceleration field is commonly assumed to remain equal to zero under quasi-static loading conditions, but not under dynamic conditions. Actually, several kinds of dynamic loading conditions can be distinguished. The first category takes inertia effects into account [40–42–62]; the second concerns tests which are performed at high speeds of loading to characterise the strain-rate sensitivity of a material, generally without inertia effects, as in the present case. Indeed, FE computations of the present tests proved that the virtual work of accelerations stay negligible compared to internal and external virtual works (ratio of about 10^3) for these small specimen masses. As a consequence, the expression (5) of the PVW is greatly simplified.

$$\underbrace{\int_{S_f} \vec{T}.\vec{u}^* \mathrm{d}S}_{w^*_{\mathrm{ext}}} = \underbrace{\int_V \bar{\sigma} : \bar{\varepsilon}^* \mathrm{d}V}_{-w^*_{\mathrm{int}}} \tag{5}$$

In the following, w^*_{int} will improperly refer to $\int_V \bar{\sigma} : \bar{\varepsilon}^* \mathrm{d}V$, so that the PVW can be simply expressed by $w^*_{\mathrm{ext}} = w^*_{\mathrm{int}}$.

The VFM [25] allows the characterisation of material models of behaviour thanks to the resolution of the PVW (Equation 5). Material parameters are introduced into Equation (5) through the expression of the stress tensor, $\bar{\sigma}$. Indeed, stresses are linked to measured strains by constitutive equations. Knowing the specimen's geometry, the applied loads and determining an appropriate virtual displacement field, the only unknowns of Equation (5) are material parameters to be identified. The PVW (4) theoretically enables the VFM to deal with all types of constitutive equations, linear or not, and all types of loadings, provided strain fields are measurable.

When dealing with nonlinear constitutive equations (plasticity, viscoplasticity, damage …), there is generally no closed-form solution linking stress and strain tensors and it is not possible to express directly the material constants using relation (5). The identification with the VFM therefore relies on the minimisation of a cost-function, φ, that expresses the discrepancy between w^*_{int} and w^*_{ext} (i.e. gap to equilibrium), as a function of the vector of unknown material parameters, $\vec{X}$. For example, φ can be defined in a least-square sense by Equation (6).

$$\varphi\left(\vec{X}\right) = \left(\frac{w^*_{\mathrm{int}}\left(\vec{X}\right) - w^*_{\mathrm{ext}}}{w^*_{\mathrm{ext}}}\right)^2 \tag{6}$$

The actual stress fields, $\bar{\sigma}$, must be known to express the internal virtual work, $w^*_{\mathrm{int}} = \int_V \bar{\sigma}\left(\vec{X}\right) : \bar{\varepsilon}^* \mathrm{d}V$. Mechanical quantities, including stress fields, are computed from full-field strain measurements by return-mapping algorithms, according to the constitutive equations of JC's viscoplastic model. In practice, time history of strain fields is measured on a finite number of time steps t_k, spread over the time period $[t_0;t_f]$. An implicit Euler scheme is used to integrate the constitutive relations and all mechanical quantities are computed at instant t_{k+1} from the total strain tensor measured at t_{k+1}, and variables previously computed at instant t_k. All plastic variables being initialised to 0 at t_0, it is advisable to perform the first measurement of strain field in an elastic state. Moreover, for the majority of available experimental techniques (e.g. DIC), the strain fields are actually analysed over the solid surfaces and strains through the thickness are not always available. In this paper, algorithms are consequently implemented assuming a plane stress condition. More details concerning the implementation of return-mapping algorithms can be found in the Appendix B. The numerical implementation was validated by comparisons with FE Analyses, using several kinds of specimens and loading conditions (explicit dynamic solver Europlexus) [44].

Strains are actually measured at a discrete set of points i, uniformly distributed according to a user-defined square mesh (step size initially equal to δ). Each point is located at the center of a subset of pixels (facets or Zone of Interest, ZOI), whose size is also defined by the user (surface generally greater than δ^2). For the computation of the internal virtual work, w^*_{int}, the volume of the Region of Interest (ROI), V_{ROI}, is divided in several sub-domains of volume V_i, external surface S_i and thickness e_i around each point of measurement i. The plane stress hypothesis allows first to consider that mechanical fields are homogeneous through the thickness of each sub-domain V_i. It is also assumed that

doi: 10.1111/str.12010

they are uniform over each surface S_i. Consequently, mechanical fields are computed by the return-mapping algorithm at each time step and in each sub-domain V_i from strains measured at point *i*. The internal virtual work is therefore computed using a discrete approximation of the integral by Equation (7).

$$w^*_{\text{int}}\left(\vec{X},t_k\right) \approx \sum_i \bar{\sigma}^i\left(\vec{X},t_k\right) : \bar{\varepsilon}^{*i} e_i(t_k) S_i(t_k) \tag{7}$$

where points *i* are the points of strain measurement (centers of ZOI).

A great advantage of the VFM is that it does not require to model precisely boundary conditions and in particular the exact repartition of loading on S_f. Indeed, as the expression (5) of the PVW is valid for any kinematically admissible virtual field, one can choose a virtual field colinear to the load resultant. The external virtual work is therefore expressed directly from the load resultant, *F*, which is measured during experiments. In the case of uniaxial tensile tests (along *y*-axis here), one can chose the simple one-dimensional virtual displacement field defined by relation (8). The expression (9) of w^*_{ext} is therefore greatly simplified, since $u^*_x = 0$ at each time step.

$$\left|\begin{array}{l} u^*_x(t_k) = 0 \\ u^*_y(t_k) = \begin{cases} 0 & \text{if } y(t_k) \le y_{\min}(t_k) \\ y(t_k) - y_{\min}(t_k) & \text{if } y(t_k) \in [y_{\min}(t_k); y_{\max}(t_k)] \\ y_{\max}(t_k) - y_{\min}(t_k) & \text{if } y(t_k) \ge y_{\max}(t_k) \end{cases} \forall t_k \end{array}\right. \tag{8}$$

where $y_{\min}(t_k)$ and $y_{\max}(t_k)$ are respectively the minimum and maximum ordinate of the ROI (i.e. zone of measurement of strain fields) at time step t_k.

$$\begin{aligned} w^*_{\text{ext}}(t_k) = \int_{S_f} \vec{T}(t_k).\vec{u}^* \mathrm{d}S &= (y_{\max}(t_k) - y_{\min}(t_k)) \underbrace{\int_{S_f} T_y(t_k)\mathrm{d}S}_{F(t_k)} \\ &= (y_{\max}(t_k) - y_{\min}(t_k))F(t_k) \end{aligned} \tag{9}$$

where S_f is characterised by $y = L$. *L* can be higher than $y_{\max}$ if the initial ROI (i.e. camera image) does not cover the whole surface of the specimen (Figure 3). Moreover, if the camera is fixed, some points of measurement, initially present in the ROI, may move off the camera field due to the deformation process, so that a reduced ROI, limited by ordinates $y_{\min}$ and $y_{\max}$ and of volume V_{ROI}, has to be considered (Figure 3). In these cases, strains are unknown on the volume domain $V - V_{\text{ROI}}$ (defined by $y \notin [y_{\min};y_{\max}]$). Yet, the expression of the internal virtual work is rewritten taking into account each subdomain of *V*, such that:

$$w^*_{\text{int}}(\vec{X},t_k) = \int_{V_{\text{ROI}}} \bar{\sigma}(\vec{X},t_k) : \bar{\varepsilon}^* \mathrm{d}V + \int_{V-V_{\text{ROI}}} \bar{\sigma}(\vec{X},t_k) : \bar{\varepsilon}^* \mathrm{d}V \tag{10}$$

where V_{ROI} is the volume associated to the reduced ROI (i.e, $y \in [y_{\min};y_{\max}]$).

As the expression (8) of the virtual field leads to a null virtual strain tensor on $V - V_{\text{ROI}}$, $\int_{V-V_{\text{ROI}}} \bar{\sigma}(\vec{X},t_k) : \bar{\varepsilon}^* \mathrm{d}V = 0$ and the internal virtual work can be computed from strain fields measured on the reduced ROI only:

$$w^*_{\text{int}}(\vec{X},t_k) = \int_{V_{\text{ROI}}} \bar{\sigma}(\vec{X}) : \bar{\varepsilon}^* \mathrm{d}V \tag{11}$$

Moreover, with the virtual field defined by Equation (8), the only component of the virtual strain tensor which is different from zero within the reduced ROI is $\varepsilon^*_{yy} = 1$, whatever the values of the actual strain components. Finally, the expression of w^*_{int} is given at each time step, t_k, by relation (12).

$$w^*_{\text{int}}(\vec{X},t_k) = \sum_i \sigma^i_{yy}(\vec{X},t_k) e_i(t_k) S_i(t_k) \tag{12}$$

with *i* the points of measurement within the ROI.

In practice, the expression (13) of the cost-function to be minimised takes into account several time steps of strain measurement, t_k.

$$\varphi(\vec{X}) = \sum_k \left(\frac{\sum_i \sigma^i_{yy}(\vec{X},t_k) e_i(t_k) S_i(t_k) - F(t_k)[y_{\max}(t_k) - y_{\min}(t_k)]}{F(t_k)[y_{\max}(t_k) - y_{\min}(t_k)]} \right)^2 \tag{13}$$

The identification of unknown parameters $\vec{X}$ with the VFM uses an iterative procedure of minimisation of the cost-function φ (Equation 13). In this paper, the algorithm of Simplex (Nelder-Mead) [54] is used. Its main advantage is that it does not require gradient computation. Nevertheless, the Simplex algorithm can converge to local minima of the non-convex cost-function. A genetic algorithm CMAES [55, 56] is therefore used at the same time to maximise the possibility of finding the global minimum of φ (Equation 13).

The iterative procedure of the VFM for the characterisation of nonlinear constitutive equations is summed up in Figure 4. It is applied in the next section to characterise the viscoplastic behaviour of alloy Ti6Al4V.

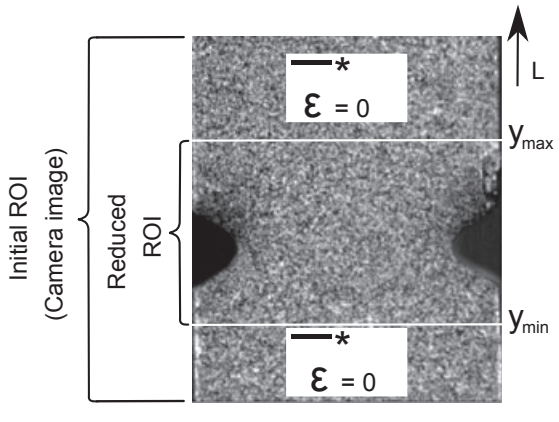

Figure 3: Camera image and reduced region of interest

Experimental Identification of the JC Model's Parameters Using the VFM

The VFM is used to identify the parameters of the JC's viscoplastic model from experimental full-field strain measurements using DIC. The method is applied to the case of a Titanium alloy (Ti6Al4V).

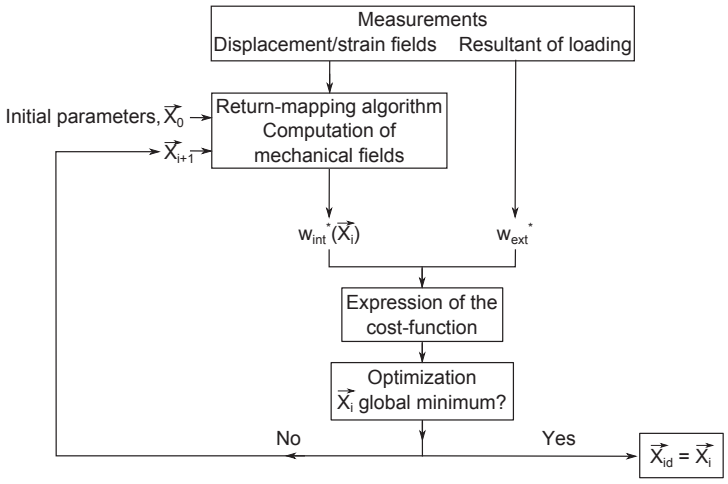

Figure 4: Iterative procedure of the virtual fields method for the characterisation of nonlinear constitutive laws

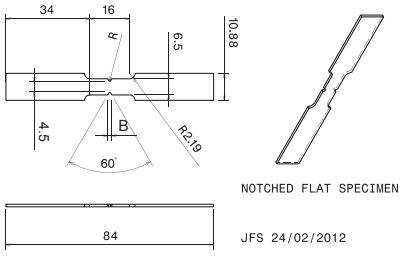

Figure 5: Notched specimen for tensile tests (all dimensions in mm, th: 1.21 mm)

Flat notched specimens (Figure 5) are taken from the same block of bulk material that has been used to manufacture the cylindrical specimens for the classical procedure of identification (Johnson–Cook's Viscoplastic Behaviour Model section and Appendix A). The notches' radius varies from 0.4 to 1.2 mm (Table 2). Specimens are subjected to tensile tests ($\vec{y}$ axis). Note that with the VFM (statically undetermined approach), there is no need to perform tests at constant strain-rate anymore, contrary to classical identification procedures (cf. Johnson–Cook's Viscoplastic Behaviour Model section and Appendix A). The initial thickness is assumed to be homogeneous all over the ROI and equal to 1.21 mm. The material is assumed to be homogeneous and elastically and plastically isotropic.

First, a tensile test is performed under quasi-static loading conditions to identify parameters governing the plastic part (i.e. strain-rate independent) of the model. Notches naturally generate heterogeneous strain-rate fields on the specimen, with a potentially large range of values. This provides therefore a rich information about the strain-rate sensitivity. In a second step, the ability of the VFM to deal with such heterogeneous mechanical fields is employed to attempt the characterisation of the strain-rate sensitivity of Ti6Al4V using only one tensile test under high-speed loading conditions.

Table 2: Notches' geometry of plate specimens

Test name	Radius of notches, R (mm)	Width of notches, B (mm)
R4	0.4	1.62
R8	0.8	2.08
R12	1.2	2.54

Characterisation of the plastic part of the model

The first tensile test is performed under quasi-static loading conditions with an imposed velocity of 5 mm min^{-1}. Conventionally, this low velocity is assumed to ensure that the equivalent viscoplastic strain-rate remains lower than the threshold, $\dot{\varepsilon}_0$, so that no viscous overstress appears in the material, according to JC's model. It was checked in the present case, even in the vicinity of the notches. In this case, the JC's isotropic hardening law is given by Equation (14) and is entirely characterised by the identification of the three parameters σ_0, K and n.

$$\sigma_y = \sigma_0 + Kp^n \tag{14}$$

Displacement/strain fields are measured using digital image stereo-correlation. This technique allows a three-dimensional representation of the surface of measurement from images of two cameras. Wu *et al.* [57] showed that the use of stereo-correlation on the front and rear faces of a thin tensile specimen simultaneously enables to reconstruct the thickness variations. In this work, stereo-correlation is used on one face of the specimens only. A plane stress state is assumed and we consider that the behaviour is identical on the opposite face. One should note that out-of-plane rigid body motions cannot be measured with one stereo-correlation system only. The assumptions give access to the evolution of the ROI's thickness in addition to in-plane strains.

doi: 10.1111/str.12010

The Region of Interest (ROI) is about 12 mm high and is centered on the plane of notches. This surface is painted in white with sprays of black paint drawing a random pattern. The ROI is divided in several subpixel zones (called facets or ZOI) characterised by their own pattern and a unique signature in grey levels. The software Aramis (Gom; GOM GmbH, Braunschweig, Germany) is used to determine the evolution of each ZOI, thanks to the recognition of its particular pattern and the comparison (i.e. correlation) with the initial undeformed state. It gives access to the deformation gradient, $\bar{F}$, used to compute the strain tensor, at the center of each ZOI, according to relation (15).

$$\varepsilon_{ij} = \frac{1}{2}(D_{ij} + D_{ji}) \tag{15}$$

with $D_{ij} = F_{ij} - \delta_{ij}$, where δ_{ij} is the Kronecker's symbol.

The ZOI size is a decisive factor in the accuracy of strain measurements by DIC [58, 59]. Indeed, using a small size of facets decreases edge effects thanks to a more precise subdivision of the ROI; however, this size must stay high enough to ensure that each facet can be characterised by a unique random pattern. On the contrary, using large facets decreases noise of measurements in low strain-range areas but does not allow to describe precisely high gradients of strain, as the measured strain is averaged over the facet. In the present case, the best compromise is obtained for a facet size of 15×15 pixels (150×150 μm^2) with a step size, δ, of 9 pixels (90 μm) in the two in-plane directions. The selection is based on strain measurements performed on a normalised unnothched specimen. First, it appears that the size of facets has no significant influence on the measurement of axial strain, ε_{yy} (Figure 6B), and that only a size of 10×10 ($\delta = 7$ pixels) leads to different values of ε_{xx} (Figure 6A). In addition, this size of facets leads to high levels of noise when measuring ε_{xy}, whereas a size of 40×40 ($\delta = 28$ pixels) leads to a too important smoothing of measurements of ε_{xy} (Figure 6C). Sizes of 20×20 pixels ($\delta = 14$ pixels) and 15×15 ($\delta = 9$ pixels) give rise to similar measurements of all strain components. Finally, the smaller size is selected because it leads to a better spatial discretisation of the ROI. Note that in Figure 6 data are extrapolated at the center of the unnotched specimen to ensure that strains are compared at the same location. In addition, analyses of rigid body motions are used to roughly evaluate uncertainties linked to facet size. Theoretically, a rigid body evolves without deformation and measured 'strains' can be considered as noise. The mean value of each measured 'strain' component is closed to 0. The standard deviation is about 10^{-4} with a ZOI of 15×15 pixels but reaches 10^{-3} for a ZOI size of 10×10 pixels. Note that these values are not raw data but those given by Aramis software that may perform a smoothing (this point was not investigated here). They may therefore be lower than conventional standard deviations encountered using raw data of DIC.

Images of the deformed surface are recorded every 0.1 s until the failure of the specimen (165 time steps). Strain fields are measured over 8002 points. The force time history

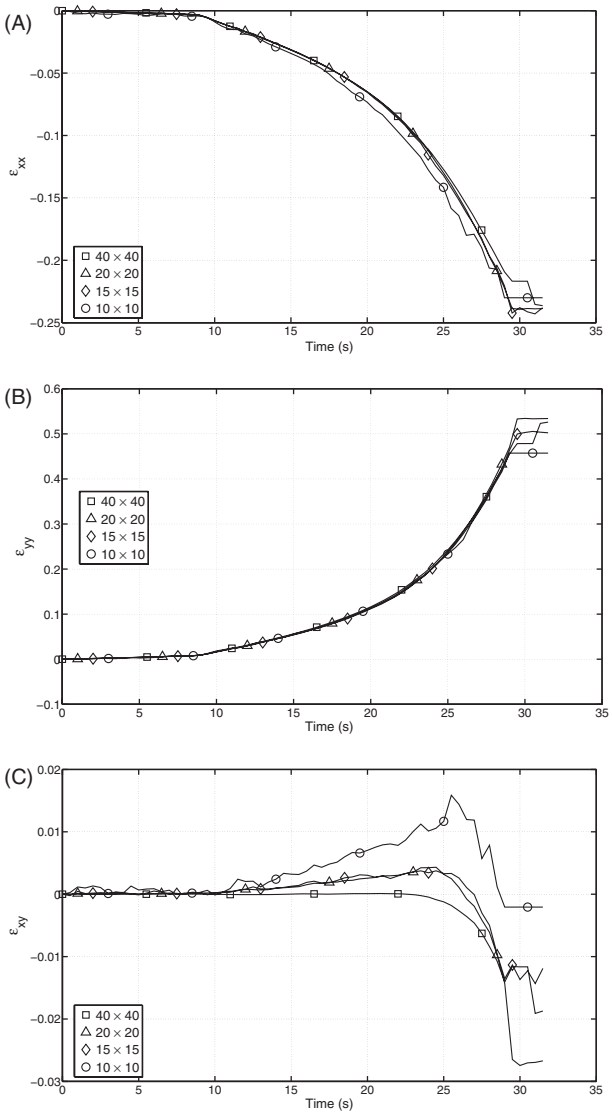

Figure 6: Influence of size of facets on measured strains – (A) ε_{xx}; (B) ε_{yy}; (C) ε_{xy}

is measured with a piezoelectric load cell (Kistler) simultaneously with image recordings. Two tests are performed for each notch radius (Table 2). The scattering of force measurement is about 3, 4 and 6% for R12, R8 and R4, respectively.

As mentioned before, stereo-correlation can give access to the thickness at the points of measurements, $e_i(t_k)$, at each instant t_k of image recording, assuming that there is no out-of-plane rigid body displacement. However, the VFM is developed so that it requires a minimum of assumptions and can be performed using simple DIC, that is, with only one camera (no stereo-correlation). So, the through-thickness strain, ε_{zz}, is also computed among other mechanical quantities by the return-mapping algorithm, in accordance with the plane stress hypothesis. For an elastic behaviour, one has $\varepsilon^e_{zz} = -\frac{\nu}{1-\nu}\left(\varepsilon^e_{xx} + \varepsilon^e_{yy}\right)$ and assuming an isochoric plastic deformation, $\varepsilon^{vp}_{zz} = -\left(\varepsilon^{vp}_{xx} + \varepsilon^{vp}_{yy}\right)$. Finally, the hypothesis of strain partition gives the expression (16) for ε_{zz}. This allows to compute the thicknesses at each point

doi: 10.1111/str.12010

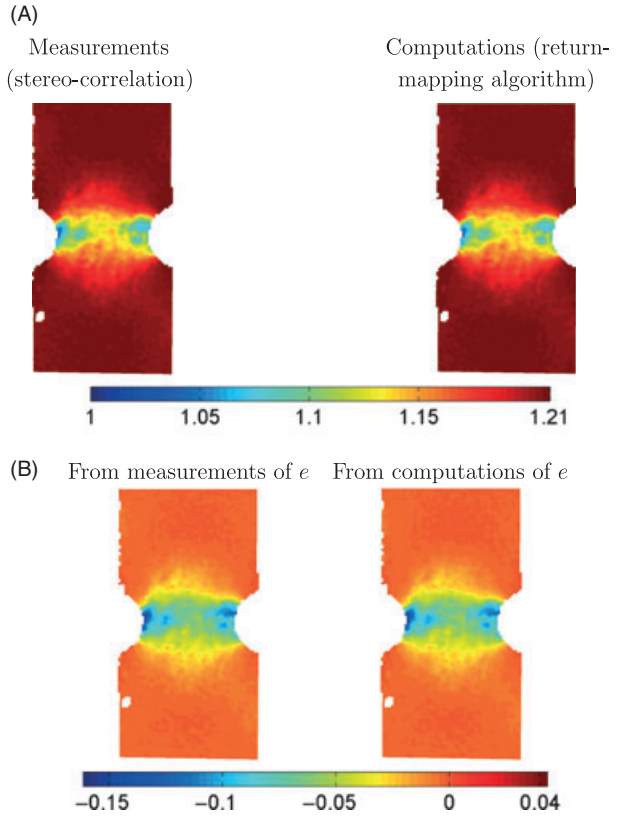

Figure 7: Thicknesses and corresponding through-thickness strains measured or computed at 14 s of quasi-static loading – (A) thicknesses; (B) ε_{zz}

of measurement, following $e_i(t_k) \approx e_0\left(1 + \varepsilon^i_{zz}(t_k)\right)$ (e_0 is the initial thickness equal to 1.21 mm).

$$\varepsilon_{zz} = -\frac{\nu}{1-\nu}\left(\varepsilon^e_{xx} + \varepsilon^e_{yy}\right) - \left(\varepsilon^{vp}_{xx} + \varepsilon^{vp}_{yy}\right) \tag{16}$$

Values of the thickness, e, computed this way or directly extracted from full-field measurements are very close to each other, as well as corresponding values of the through thickness strain, ε_{zz}. For example, the average gap between values of ε_{zz} computed from 'measured' thicknesses or by the return-mapping algorithm following plane stress hypothesis (16) is of 3.8 10^{-4}. This gap corresponds to a relative deviation of 2.8% with regard to the average value of ε_{zz} over the ROI (−1.37 10^{-2}) at 14 s of loading (Figure 7). These results validate the experimental protocol for strain measurement, including plane stress hypothesis. Note that

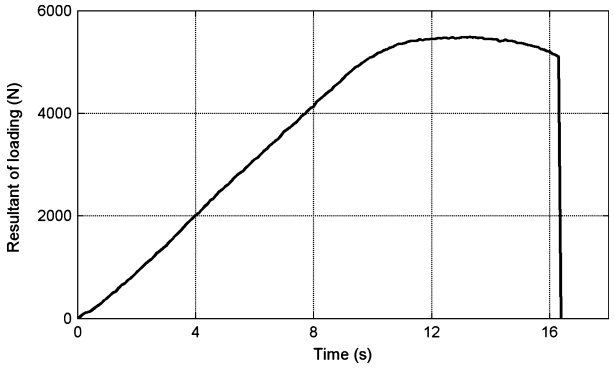

Figure 8: Applied load during the quasi-static tensile test

the thickness is decreased of about 17% in the vicinity of notches of R12 specimen (through thickness necking), at 14 s of loading (Figure 7A).

Force and strains time history (Figures 8 and 9, respectively) measured during quasi-static loading of a specimen *R*12 are used to identify plastic parameters (σ_0, K and n) of JC's model (Equation 14) with the VFM. Figure 9(A) and (B) give respectively an example of in-plane strains measured at 14 s of loading (imposed displacement along axis $\vec{y}$ of about 1.16 mm) and their time history for a point located at the vicinity of the notch (area of strain localisation). The one-dimensional virtual displacement field (8) is used to express the cost-function, φ (13), to be minimised. Surfaces S_i are computed thanks to initial coordinates and measured displacements of points i. The expression (13) of φ uses the strain maps number 1–140 (0.1–14 s) which correspond to a sufficient development of strain hardening in the material to enable its characterisation. At this stage of loading, the cumulated plastic strain is higher than 0.2 in the vicinity of the notches and is about 0.07 at the center of the ROI. The slight decrease of F (Figure 8) observed from step number 140 can be the sign of a significant development of necking and/or damage in the material, which would violate the plane-stress hypothesis or make the use of JC's model not appropriate anymore. It explains why steps after number 140 are not taken into account to express φ. In addition, there may be a significant loss of data during loading (Figure 10), mainly because of edge points that move off the camera's field. Consequently, the ROI is reduced to about 4 mm height, for which loss of data is negligible.

The initial values of parameters used in the optimisation process (Figure 4) are respectively equal to 500 MPa for σ_0 and K and 1 for n. The cost-function $\varphi\left(\vec{X}\right)$ (Equation 13) is minimised by the Simplex and CMAES algorithms. Both algorithms converge properly, with final values of $\varphi\left(\vec{X}\right)$ very close to each other (Table 3). Moreover, both algorithms find the same value for the initial yield stress and hardening moduli and exponents differ only by 0.7%. Obviously, Simplex and CMAES algorithms lead to similar identified behaviours. From now on, the values of plastic parameters identified with the VFM are considered to be those found by Simplex algorithm, as the corresponding value of $\varphi\left(\vec{X}\right)$ is slightly lower than for the CMAES algorithm.

It is worth noting that the identified value of 899 MPa for the initial yield stress, σ_0, is consistent with values found in the literature for Ti6Al4V [46, 60]. Nevertheless, it is lower than the value identified with the classical procedure (973 MPa, Table 1). This gap can be due to some heterogeneities in the cold-forged block of Ti6Al4V used both to manufacture the specimens for the classical procedure (Johnson–Cook's Viscoplastic Behaviour Model section and Appendix A) and for the VFM. A means to verify the relevance of the identified plastic parameters, $\vec{X}_{id}$ (Table 3 – Simplex) is to compare the computed and measured forces. The force can be computed at all the levels of ordinate (with $\vec{y}$ the tensile axis), except at the upper boundary of the initial ROI (12 mm), because of the important loss of data due to points located initially at the

doi: 10.1111/str.12010

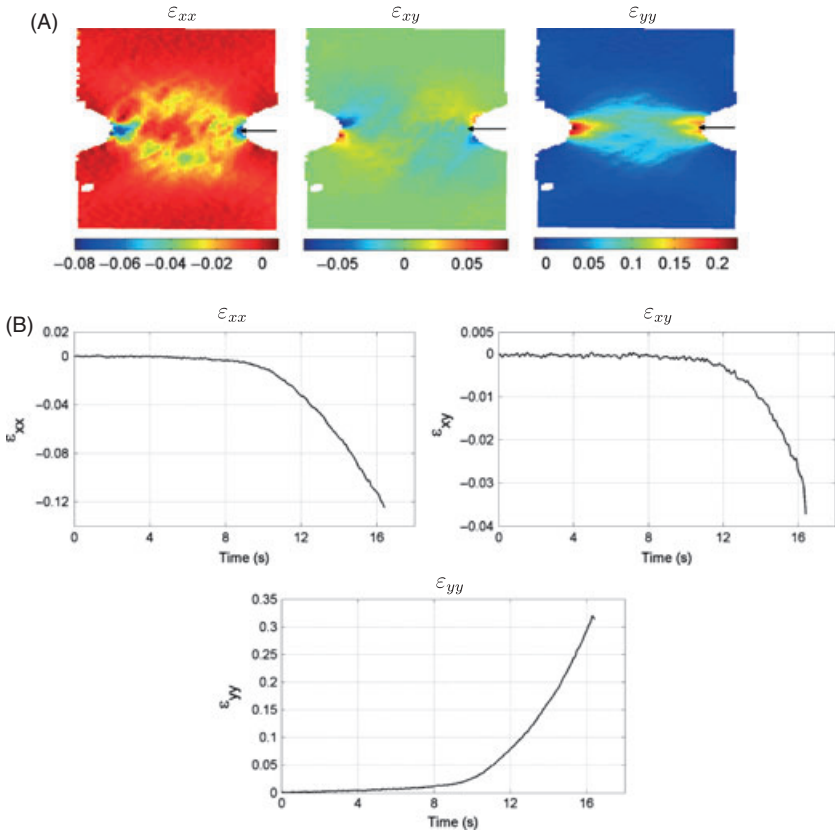

Figure 9: In-plane strains measured during quasi-static tensile loading – (A) spatial distributions at 14 s; (B) time histories – vicinity of the notch (location pointed by arrows)

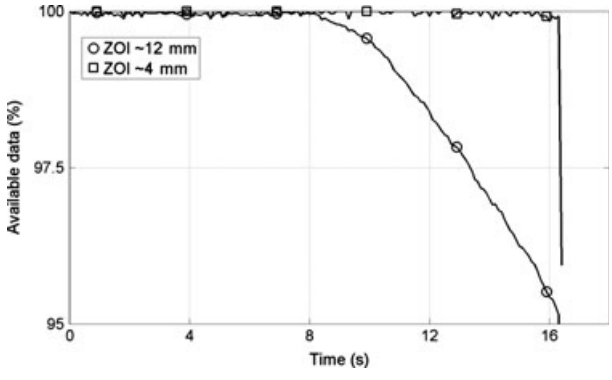

Figure 10: Loss of data during quasi-static tensile test

top of the image and moving off the camera during the elongation of the notched specimen. To avoid the subjective selection of one or more levels of ordinate among the large amount of data, the computed force, $<F_\sigma>$, is actually defined by the relation (17) as the average force acting over the ROI. Note that it is consistent with the use of integrals in the expression of the cost-function (global expression). In the relation (17), stresses are obviously calculated with the return-mapping algorithm considering parameters $\vec{X}_{id}$.

$$< F_\sigma(t_k) >= \frac{\sum_i \left[\sigma^i_{yy}(\vec{X}_{id}, t_k) e_0 (1 + \varepsilon^i_{zz}(t_k)) S_i(t_k)\right]}{y_{\max}(t_k) - y_{\min}(t_k)} \quad \forall t_k \qquad (17)$$

with i the points of measurement inside the ROI.

Figure 11(A) allows to compare the values of the load resultant, $<F_\sigma>$, computed using Equation (17), to the measured one, F, for specimen R12 (used in the process of identification), for both 12 and 4 mm-high ROIs. $<F_\sigma>$ is also computed for specimens R8 and R4 (Figures 11B,C, respectively). In all cases, the temporal evolutions of the computed forces with identified plastic parameters are consistent with the measurements of F. It can be noted that values of $<F_\sigma>$ computed by Equation (17) are slightly higher than F in the case of the ROI of 4 mm of specimen R4. It is mainly due to a more important strain concen-

Table 3: Characterisation of plastic part of Johnson–Cook's model with the virtual fields method

Algorithm	Identified parameters			Final value of φ (Initial value: 1.9726)	Number of evaluations
	σ_0 (MPa)	K (MPa)	n		
Simplex	899	524	0.5935	0.2853344	744
CMAES	899	520	0.5893	0.2853345	2695

doi: 10.1111/str.12010

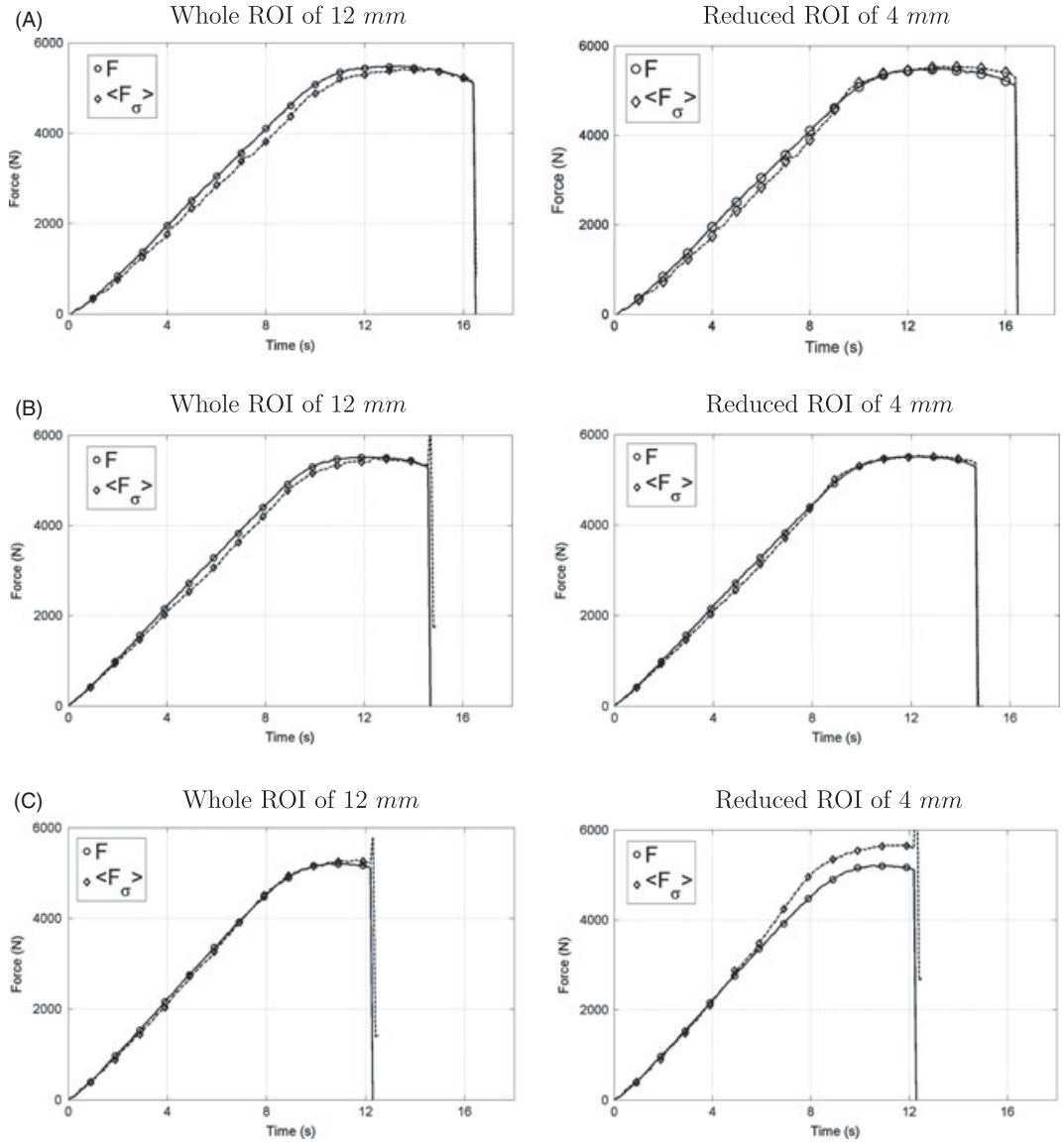

Figure 11: Computations of forces with identified values of material parameters – quasi-static test – (A) test R12; (B) test R8; (C) test R4

tration at the vicinity of notches, sharper for this specimen, that leads to higher average values of stresses on the ROI of 4 mm, whereas they are of the same magnitude than for other specimens for the ROI of 12 mm. It explains why computed values of $<F_\sigma>$ by Equation (17) are higher than F on the ROI of 4 mm whereas they are very closed to each other for the ROI of 12 mm.

These results demonstrate that the plastic part, i.e. strain-rate independent, of JC's model, can be characterised experimentally with the VFM. The next step is to apply the VFM to full-field strain measurements under higher speed loading conditions to characterise the strain-rate sensitivity of Titanium alloy Ti6Al4V.

Characterisation of the strain-rate sensitivity of Ti6Al4V

Under the higher velocity of 0.2 m s^{-1}, the strain-rate dependent part of the JC's isotropic hardening law (18) models the development of viscous effects in the material. The characterisation of the strain-rate sensitivity requires the identification with the VFM of the viscoplastic parameters, M and $\dot{\varepsilon}_0$.

$$\sigma_y = (\sigma_0 + Kp^n)\left(1 + M\ln\left(\frac{\dot{\varepsilon}_{eq}^{vp}}{\dot{\varepsilon}_0}\right)\right) \quad (18)$$

It is worth noting that in the vast majority of procedures of characterisation of JC's viscoplastic model [46, 49] the value of the viscoplastic threshold, $\dot{\varepsilon}_0$, is arbitrarily fixed (generally at 1 s^{-1}) and the strain-rate sensitivity is characterised with the identification of parameter M only. This approach is relevant because the phenomenological JC's model [21] does not aim to model the plastic-viscoplastic transition but is dedicated to the description of the material behaviour under high strain-rates, thus allowing to relativize the physical sense attributed to the viscoplastic threshold. Indeed, under high strain-rates, viscous effects are developed with certainty in the material and strain-rate sensitivity can actually be described by the only parameter M. In this study, it was chosen to identify both viscoplastic

doi: 10.1111/str.12010

parameter, M, and strain-rate threshold, $\dot{\varepsilon}_0$, with the VFM. As briefly highlighted in Appendix A, it raises the problem of the uniqueness of the couple of parameters. Nevertheless, the aim is to demonstrate that a viscoplastic behaviour can be entirely characterised by the VFM, without needing any arbitrary choice by the user. Note that it remains possible to fix the value of the threshold in the process of the VFM to identify M only (cf. Relevance of the JC's model characterised with the VFM section).

Specimen R4 (Figure 5 and Table 2) is subjected to tensile loading at the imposed velocity of 0.2 m s^{-1} using a hydraulic jack (Figure 12). Displacement/in-plane strain fields are measured by DIC (camera Photron RS2000), with a frequency of acquisition of 10 kHz. The ROI height is about 7 mm (Figure 13). Its thickness is assumed to be homogeneous before loading and $e_0 = 1.21$ mm. The force time history is measured by a piezoelectric load cell at the higher frequency of 1 MHz. In the post-treatment, only values measured simultaneously with image recording are taken into account. Again, the size of facets is a decisive factor. Note that the actual surface covered by a facet is greater in the present dynamic loading conditions than in the previous quasi-static conditions, for the same number of pixels (210×210 μm^2 compared to 150×150 μm^2 for a facet of 15×15 pixels). It is due to a lower resolution of the camera because of the higher frame rate. Moreover, unsatisfying high levels of noise are encountered with a size of facets of 15×15 pixels for this dynamic loading. The size of 20×20 pixels (280×280 μm^2) that gives rise to the best compromise is therefore selected ($\delta = 12$ pixels). 64 maps of strains of 1106 points of measurement are recorded until the failure of the specimen (i.e. total imposed displacement of 1.28 mm). It is worth noting that there is no loss of data during loading. In fact, the image is initially higher than the measurement area and no point moves off the camera's field during the dynamic test.

Because of the larger dimensions of the ZOI and the lower density of points of measurements than in quasi-static conditions ($\delta = 168$ μm in dynamic conditions, compared to 90 μm in quasi-static conditions), the ROI is roughly approximated by its sub-division into ZOI. This point is illustrated by Figure 14 that allows to compare the spatial distribution of points of measurement for the specimen $R4$ in quasi-static and in dynamic loading conditions (facets were not drawn to keep a readable figure). An important consequence is that a part of the surface is 'missing' on the lateral edges as the current spatial parameters lead to a bad estimation of the total surface of the ROI, $S = \sum_i S_i$, where S_i is the surface associated with the point of measurement i. Quantitatively, the value of S_{Dynam}, computed at the initial step (i.e. undeformed) of dynamic loading, is about 34.50 mm^2. In comparison, the value of S_{QS}, computed at the initial step of quasi-static loading (size of facets of 150×150 μm^2), for the same height of ROI, is about 37.95 mm^2. This latter is close to the actual surface of ROI evaluated to about 39 mm^2. This underestimation of S_{Dynam} directly affects the computation of w^*_{int} by Equation (12). Obviously, it introduces an important bias in the expression (13) of the cost-function, as the problem is stated as if the applied force was virtually

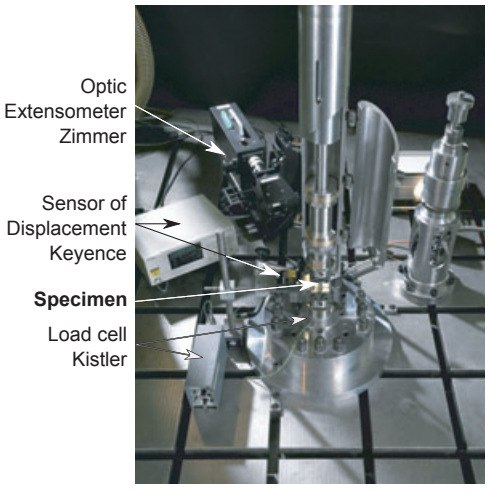

Figure 12: Set-up for dynamic tensile test

Figure 13: Region of interest of specimen $R4$

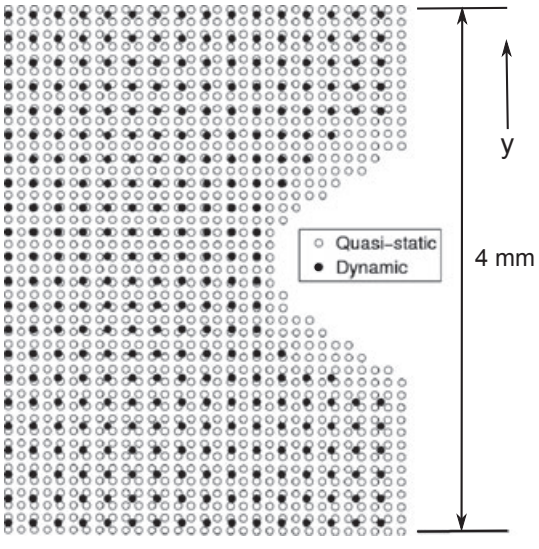

Figure 14: Spatial distribution of points of measurement under quasi-static and dynamic loading conditions – specimen $R4$

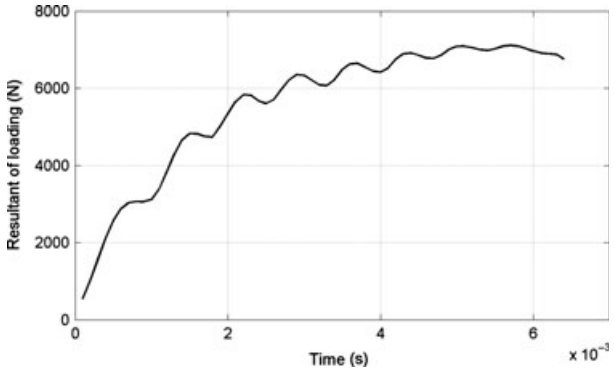

Figure 15: Applied load during the dynamic tensile test

concentrated in a reduced surface. A solution to limit the effect of loss of value of ROI's total surface is to introduce a surface corrective factor that leads to the modified expression (19) of the internal virtual work.

$$w_{\text{int}}^{*Corr} = \underbrace{\sum_i \sigma_{yy}^i\left(\vec{X},t_k\right)e_i(t_k)S_i(t_k)}_{w_{\text{int}}^{*}\left(\vec{X},t_k\right)} \frac{S_{\text{QS}}}{S_{\text{Dynam}}} \tag{19}$$

It can be seen from Figure 15 that measured values of the load resultant, F, are affected by the natural frequency of the set-up, as well as strains (Figure 16A with $\vec{y}$ the tensile axis). Levels of strains can be very different depending on the location on the specimen. Figure 16 gives another example of the heterogeneity of strain fields. Thanks to the presence of notches, strain-rate fields are also strongly heterogeneous. This allows to characterise the strain-rate sensitivity of the Ti6Al4V alloy with the VFM from this single dynamic test. Note that strain-rate of about 300 s^{-1} can be reached locally, even for the quite low tensile velocity of 0.2 m s^{-1} (Figure 17, at the end of dynamic loading). It is worth noting that the strain-rate is computed at each point of measurement by the return-mapping algorithm as the ratio of the equivalent strain's increment (equal to $\frac{3}{2}\Delta p$) by the time step. The use of several levels of loading to build the cost-function also allows to expand the range of considered strain-rate and to follow the potential transition from plastic to viscoplastic behaviour at all points of measurement.

The cost-function, φ, is expressed by Equation (13) considering the corrected expression (19) of the internal virtual work. Data from every 1106 points included in the ROI and all of the 64 time steps are taken into account. Stresses are computed by the return-mapping algorithm with the values of plastic parameters, σ_0, K and n, previously identified

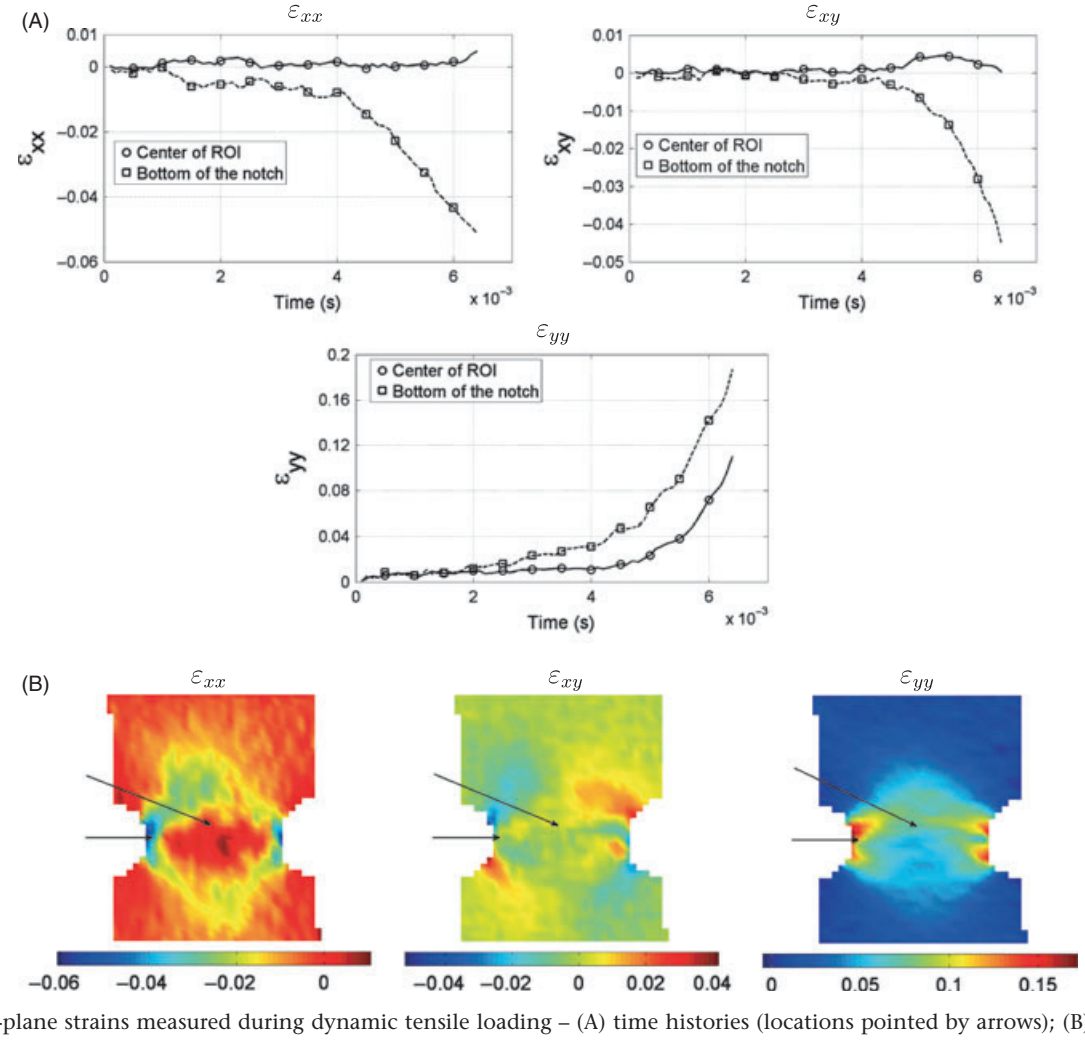

Figure 16: In-plane strains measured during dynamic tensile loading – (A) time histories (locations pointed by arrows); (B) spatial distributions at 6 ms

doi: 10.1111/str.12010

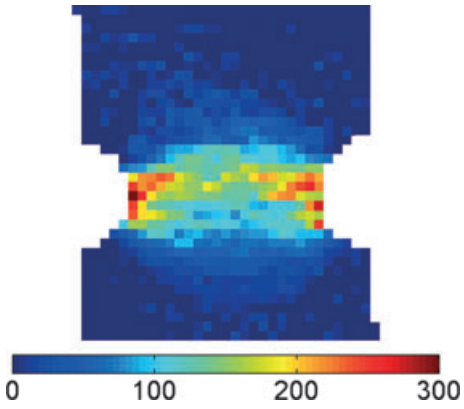

Figure 17: Strain-rate field at the end of dynamic loading

by the VFM (see Characterisation of the plastic part of the model section, Table 3). Results of minimisation of φ are listed in Table 4(A). The results are quite close to each other for both algorithms of optimisation. Identified values of material parameters, $\vec{X}_{id}$, are 0.0470 and 0.1733 s^{-1} for M and $\dot{\varepsilon}_0$, respectively.

Again, these values of viscoplastic parameters can be validated by comparing measured values of the load resultant, F, to computed ones. In this dynamic case, the number of points of measurement is lower than in quasi-static conditions and it is easy to compute the load that is applied on each row of ordinate y, according to expression (20), all the more because there is no loss of data.

$$F_\sigma(t_k, y) = \sum_i \sigma^i_{yy}\left(\vec{X}_{id}, t_k\right) e_i(t_k) \Delta x_i(t_k) \quad \forall t_k \tag{20}$$

where points i are the points of measurement of ordinate y. Δx_i is the width (in the $\vec{x}$ direction) of the surface S_i surrounding point i.

Stresses are computed by the return-mapping algorithm for identified values of material parameters, $\vec{X}_{id}$. Figure 18

Table 4: Identification of viscoplastic parameters with the virtual fields method – (A) results of optimisation; (B) relative gaps between computed and measured force

(A)

Algorithm	Identified parameters		Final value of φ (Initial value : 0.5968)	Number of evaluations
	M	$\dot{\varepsilon}_0$ (s^{-1})		
Simplex	0.0448	0.1524	0.1323	358
CMAES	0.0470	0.1733	0.1316	910

(B) Values of τ %

Top boundary (y_{max})	Notches	Intermediate	Average on all values of y
8.67	14.12	8.13	3.20

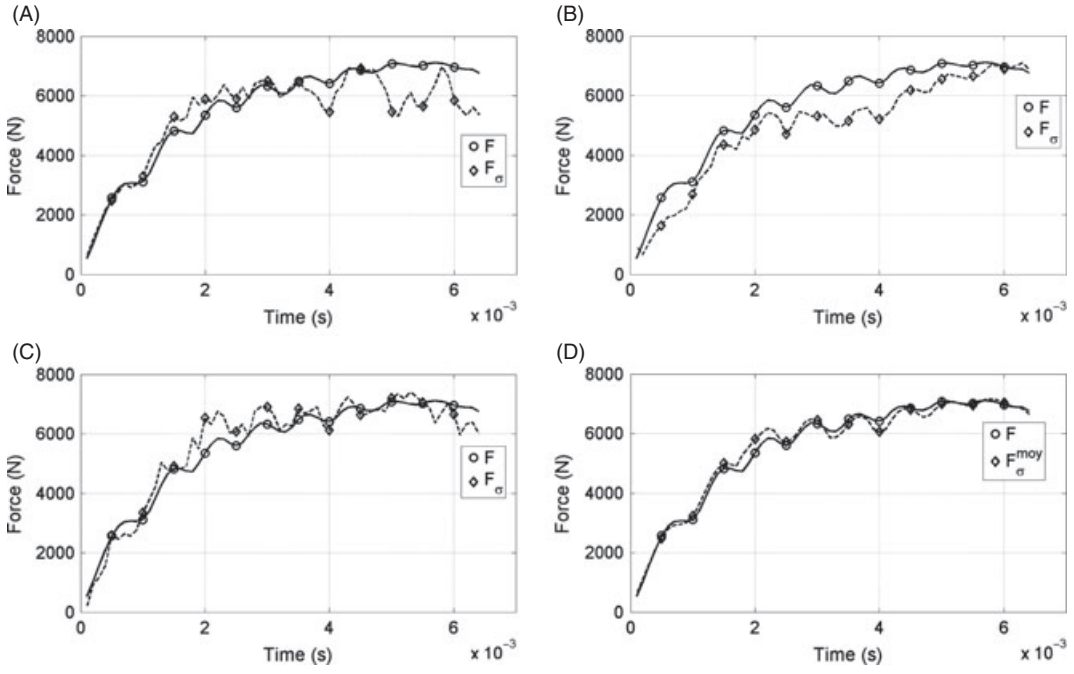

Figure 18: Computations of forces with identified values of material parameters – dynamic test – (A) upper boundary of the region of interest (y_{max}); (B) vicinity of the notch; (C) intermediate ordinate; (D) average for all values of y

doi: 10.1111/str.12010

Table 5: Identification of viscoplastic parameters without the surface corrective factor – (A) results of optimisation; (B) relative gaps between computed and measured force

(A)

Algorithm	Identified parameters		Final value of φ (Initial value: 0.5148)	Number of evaluations
	M	$\dot{\varepsilon}_0$ (s^{-1})		
Simplex	0.0832	0.1078	0.2952	2002
CMAES	0.0656	0.0157	0.2789	1997

(B) Values of τ (%)

Top boundary (y_{max})	Notches	Intermediate	Average on all values of y
11.93	17.85	9.30	5.01

shows that computed values of F_σ, for several values of y, as well as the average value of F_σ for all ordinates, F_σ^{moy}, are close to measured values, F. Table 4(B) shows the computed average gaps, τ, between F and F_σ throughout dynamic loading, following relation (21). In particular, relative gap between F_σ^{moy} and F is only about 3.2%. As expected, discrepancies are higher at the ordinate of the notches. Indeed, this area of strain localisation is logically the most affected by the problem of spatial resolution which can lead to a bad evaluation of high gradients of strain.

$$\tau = \underset{k}{\text{mean}}\left[\text{abs}\left(\frac{F_\sigma(t_k, y) - F(t_k)}{F(t_k)}\right)\right] \tag{21}$$

Note that the viscoplastic parameters can also be identified without any surface corrective factor. In this case, the identified values of the viscoplastic parameters are different from $\vec{X}_{id}$ and are now highly dependent on the algorithm used (Table 5a). Moreover, the final values of the cost-function are more than twice as high as when using the corrective factor. It may reveal that the simple use of the surface corrective factor immediately leads to a more pronounced global minimum of φ and to an improvement of the robustness of the identification. In addition, the relative gap, τ, is higher whatever the ordinate considered to compute F_σ and is now about 5% for F_σ^{moy} (Table 5b).

These results demonstrate the ability of the VFM to characterise the viscoplastic part of JC's model of behaviour, using only one tensile test under high-speed loading conditions. An other interesting property of the VFM is that it does not require any smoothing of the measured force time history, even if it presents important oscillations (as frequently observed in dynamic loading conditions, Figure 15). One can note that tests of identification (not described here) using the VFM with smoothed load's time histories lead to less satisfying results. In fact, the integrals in the expression (13) of the cost-function act somewhat as filters but treating the internal and external virtual works simultaneously, thus limiting the alteration of data. Last, the use of a surface corrective factor, when a rough subdivision of the ROI leads to a bad estimation of its total surface, allows to improve the accuracy of the identification. The relevance of the whole JC's model characterised by the VFM to describe the behaviour of alloy Ti6Al4V is discussed in the next section.

Discussion

Relevance of the JC's model characterised with the VFM

Table 6 summarised the identified values of JC's parameters for Ti6Al4V with the VFM and with the classical procedure of statically determined tests (cf. Johnson–Cook's Viscoplastic Behaviour Model section and Appendix A). The aim is not to discredit one of the two identified sets of material parameters as processes (specimens, kinds of measured data …) are too different. Then, as underlined before, specimens are extracted from a block of Ti6Al4V which may be heterogeneous, that can explain some differences between the two identified behaviours. The two identified values of the initial yield stress, σ_0, are quite different. Finding out a lower value of the initial yield stress when using DIC is consistent with possible problems of spatial resolution (bad estimation of high strain gradients) raised by this method of measurement. Nevertheless it does not explain entirely this important gap. Note that the value of 899 MPa, identified with the VFM, is closer to common values encountered in the literature (e.g. 896 MPa for Meyer and Kleponis [46]). Last, identified values of hardening parameters are very close to each other for the two characterised models.

Table 6: Identified values of Johnson–Cook's parameters for Ti6Al4V

	Virtual fields method	Classical procedure (statically determined tests)
Initial yield stress, σ_0 (MPa)	899	973
Isotropic hardening modulus, K (MPa)	524	557.3
Isotropic hardening exponent, n	0.5935	0.5632
Viscoplastic strain-rate threshold, $\dot{\varepsilon}_0$ (s^{-1})	0.1733	1.29
Viscoplastic parameter, M	0.0470	0.0329

doi: 10.1111/str.12010

As exposed in sections Johnson–Cook's viscoplastic behaviour model and Characterisation of the strain-rate sensitivity of Ti6Al4V, common values of the viscoplastic threshold, $\dot{\varepsilon}_0$, are about 1 s^{-1} in the literature [46, 49]. It is worth reminding that it was the reason why the value of 1.29 s^{-1} was selected during the exploitation of statically determined tests (cf. Appendix A) although a lower value of 5.37 10^{-2} s^{-1} led to a better coefficient of determination. As underlined before, this arbitrary choice of the value of 1 s^{-1} for the viscoplastic threshold is relevant when the aim is to characterise the material behaviour under high strain-rates, because viscous effects are developed with certainty in the material and the strain-rate sensitivity can be described by the only parameter M (Equation 18). Obviously, the VFM can be applied following this approach. In this way a value of 0.0747 is identified for parameter M when $\dot{\varepsilon}_0$ is fixed to 1 s^{-1} (same procedure as that described in Characterisation of the strain-rate sensitivity of Ti6Al4V section, using the surface corrective factor; final value of φ, expressed by Equation (13), of 0.1379 for both Simplex and CMAES). Thanks to coupled effects of viscoplastic parameters in the hardening law (18) at high strain-rates, this higher value of M offsets the higher value of $\dot{\varepsilon}_0$, so that computed values of σ_{yy}, for example, and F_σ^{moy} (by Equation 20) are very close to each other for both values of viscoplastic threshold and associated parameter M (Figure 19).

Again, these observations underline the lack of uniqueness of the couple of viscoplastic parameters, M and $\dot{\varepsilon}_0$, which characterise the strain-rate sensitivity of a material according to the phenomenological model of JC. Moreover, the weight of the viscous part in the hardening law (18) is generally less important than that of the strain-hardening, except at very high strain-rates. As a consequence, a variation of the values of viscoplastic parameters does not affect significantly the global material behaviour and their identification becomes therefore a challenge difficult to face. To illustrate this fact, Figure 20 shows the values of the cost-function computed using Equation (13) for a large range of values of viscoplastic parameters, using the 64 maps of strain measurements of the dynamic loading (Characterisation of the strain-rate sensitivity of Ti6Al4V section) and the identified values of plastic parameters (Table 3). It clearly shows that the low weight of viscoplastic parameters causes significant plateaus of the VFM's cost-function. The results of identification are therefore obviously very sensitive to all the biases that can affect the computation of the cost-function. Note that it can be verified on Figure 20 that the identified couple of viscoplastic parameters (Table 4a) really corresponds to a minimum of the cost-function.

Actually, this discussion raises the limits of the modelling of a material strain-rate sensitivity by the phenomenological JC's model. It underlines that the identification of viscoplastic parameters may be very challenging, whatever the method of identification used. Nevertheless, the VFM enables to find the value of the viscoplastic parameter M which is the most appropriate to describe the material dynamic behaviour, whatever the imposed value of viscoplastic threshold. In addition, it was demonstrated that the VFM allows the identification of the two viscoplastic parameters simultaneously, so that no subjective choice of the user is required. Indeed, simultaneously identified values of M and $\dot{\varepsilon}_0$ (Table 6) were proven to allow a good

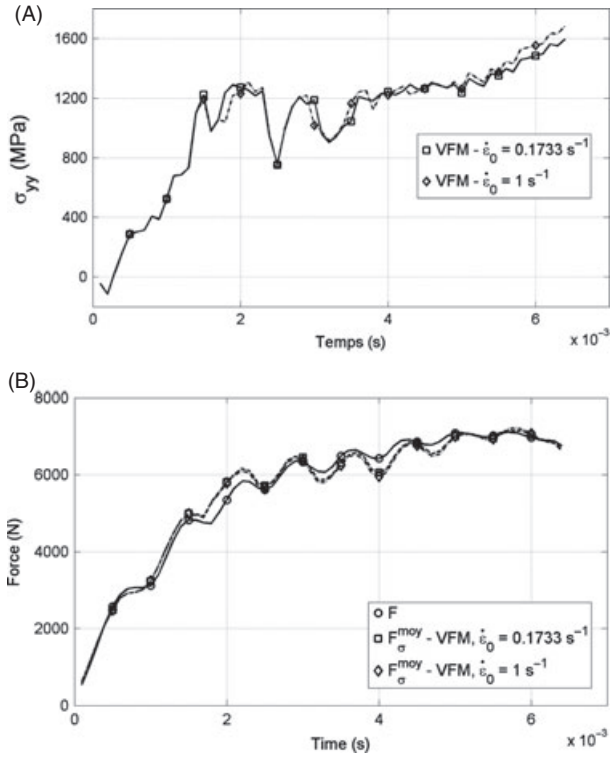

Figure 19: Influence of fixed value of $\dot{\varepsilon}_0$ on mechanical fields computed during dynamic loading – (A) σ_{yy} (vicinity of the notch); (B) F_σ^{moy}

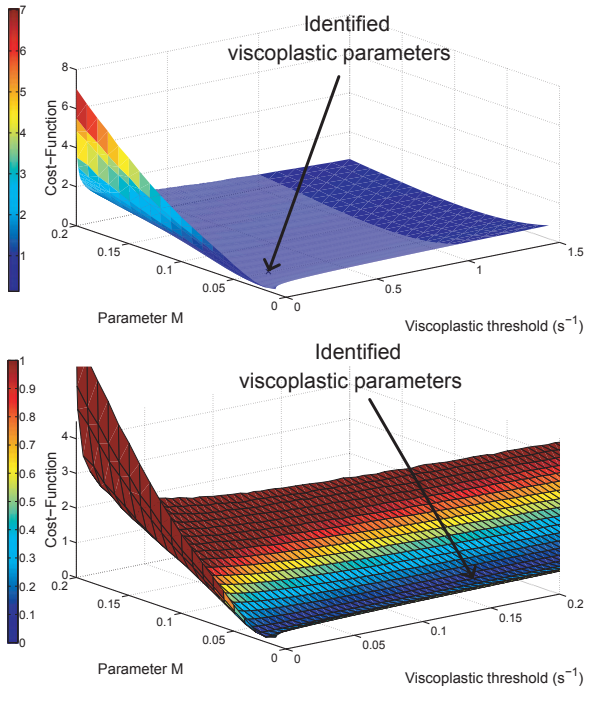

Figure 20: Influence of the values of viscoplastic parameters on the cost-function

description of the strain-rate sensitivity of Ti6Al4V. Yet, there is no possibility to judge the physical sense of a value of 0.1733 s^{-1} for $\dot{\varepsilon}_0$. Again, it is worth reminded that because of the phenomenological character of the JC's model the analysis of the physical sense of $\dot{\varepsilon}_0$ is not necessarily relevant. Anyway, a means to give it a physical sense might be to perform several statically determined tensile tests at gradually increased strain-rate to locate approximately the beginning of the development of viscous effects on the strain-stress response.

Influence of DIC's spatial resolution on the characterisation with the VFM

As already mentioned in the previous sections, the choice of the spatial parameters of the DIC (in particular step size, δ, and size of ZOI) can affect the accuracy of strain field measurements as well as the computation of the internal virtual work (e.g. because of a bad subdivision of the ROI). It can therefore obviously influence the results of identification with the VFM.

To quantify the influence of DIC's spatial parameters, the images recorded during the quasi-static tensile test of the specimen *R*12 (see Characterisation of the plastic part of the model section) are processed again using the software Aramis with different values of size of ZOI and of δ to extract the strain fields. Sizes of ZOI of 20 pixels, with δ equals to 10 and 14 pixels, 30 pixels ($\delta = 10$ pixels) and 40 pixels ($\delta = 10$ and 28 pixels), arbitrarily chosen, are tested (Table 7). Figure 21 shows the axial strain, ε_{yy}, computed for each couple of spatial parameters at 14 s of loading (imposed displacement of 1.17 mm) on 4 mm-high ROIs. In the legend, and in all the following, the first number in pixels stands for the size of the ZOIs, the second stands for the value of δ (step size, i.e. gap between points of measurement). Obviously, high values of δ lead to a roughly divided ROI and to an important underestimation of its total surface (Table 7). Then, as expected, large sizes of ZOI lead to an underestimation of strain in the areas of localisation because of an excessive smoothing (averaging) of high strain gradients.

The VFM is processed using these new strain fields to characterise the rate-independent part of JC's model. The conditions of identification are identical to those previously used (cf. Characterisation of the plastic part of the model section). In particular, the ROI is high of 4 mm and the cost-function, φ, is expressed by Equation (13) using the 140 first maps of strain, without any correction of surface. Table 8(A) allows to compare the results of identification for all new sets of DIC's spatial parameters to the previous ones obtained for spatial parameters of 15×9 pixels. Note that identified parameters are always identical whatever the algorithm of optimisation used. The identified values of the initial yield stress, σ_0, are quite close to each other for ZOI of 15 and 20 pixels but are strongly overestimated for facets of 30 and 40 pixels. The reason is that higher identified values of σ_0 allow to offset the lower levels of strains measured by DIC with large sizes of facets. Hardening parameters K and n are affected similarly. Each set of identified parameters is used by the return-mapping algorithm to compute stress fields and the average force acting on the ROI, $<F_\sigma>$, by Equation (17) (Figure 22A). Average relative gaps between $<F_\sigma>$ and the measured force, F, are computed following the relation (22) and are listed in Table 8(B).

$$< \tau >= \underset{k}{\text{mean}}\left[\text{abs}\left(\frac{< \mathrm{F}_\sigma > (\mathrm{t_k}) - \mathrm{F}(\mathrm{t_k})}{\mathrm{F}(\mathrm{t_k})}\right)\right] \quad (22)$$

The largest size of ZOIs logically leads to the highest average gap between measured and computed forces.

Table 7: Spatial parameters of digital image correlation – quasi-static loading of specimen *R*12

Size of ZOIs (pixels)	δ (pixels)	Number of points of measurement	Initial surface of the ROI (mm^2)
15	9	2414	20.7194
20	10	1947	20.5505
20	14	1018	20.5523
30	10	1890	19.933
40	10	1832	19.2818
40	28	251	18.3979

ZOI, zone of interest; ROI, region of interest.

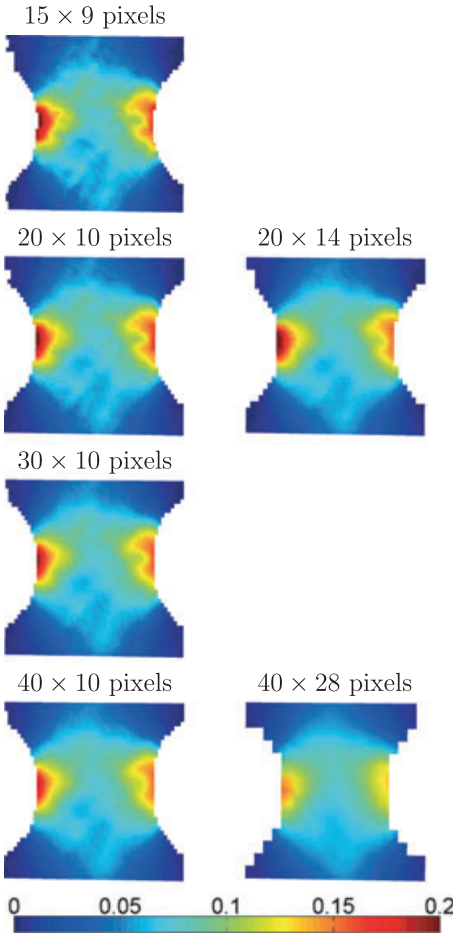

Figure 21: Influence of the spatial parameters of digital image correlation on computed axial strains (14 s of quasi-static loading of specimen *R*12)

doi: 10.1111/str.12010

Table 8: Influence of spatial parameters on the identification with the virtual fields method – quasi-static loading of specimen *R*12 – (A) results of identification; (B) average relative gaps between measured and computed forces

(A)

Spatial parameters of DIC (pixels)	Identified parameters			Final value of φ	Number of evaluations
	σ_0 (MPa)	K (MPa)	n		
15 × 9	899	524	0.5935	0.2853	744
20 × 10	894	439	0.5055	0.3189	479
20 × 14	895	480	0.5301	0.3563	708
30 × 10	922	578	0.6274	0.4890	522
40 × 10	956	714	0.7420	0.7302	518
40 × 28	1013	935	0.8843	1.373	564

(B)

Spatial parameters of DIC (pixels)	15 × 9	20 × 10	20 × 14	30 × 10	40 × 10	40 × 28
$<\tau>$ (%)	5.23	5.54	5.81	6.84	8.34	11.63

DIC, digital image correlation.

Obviously, the higher the density of points of measurement, the greater the accuracy of identification for a same size of ZOIs.

Figure 22(B) shows that the gaps between F and $<F_\sigma>$ are concentrated in the first stages of loading, before about 9.5 s. It corresponds to strain maps where the plastic flow has not begun for the vast majority of points. In this case, the underestimation of strains due to unsuitable DIC parameters directly leads to underestimated stresses, because of linear elastic laws and fixed elastic parameters and therefore to underestimated computed forces. Then, during the plastic phase, the process of the VFM aims to minimise the discrepancy between the internal and external virtual works by adjusting the values of identified plastic parameters. As a consequence, the underestimation of strains is offset by the overestimation of plastic parameters (Table 8 a) and the gaps between F and $<F_\sigma>$ strongly decrease. Indeed, the average gaps $<\tau>$ (22) computed for the last stages only (i.e. k varying from 95 to 140) are <0.75% for all sets of DIC's spatial parameters. These results prove again that the VFM is able to find the values of material parameters that are the most consistent with experimental data. However, if these data are biased (e.g. underestimation of strain), the results of identification with the VFM will inevitably be biased too, as with any other method.

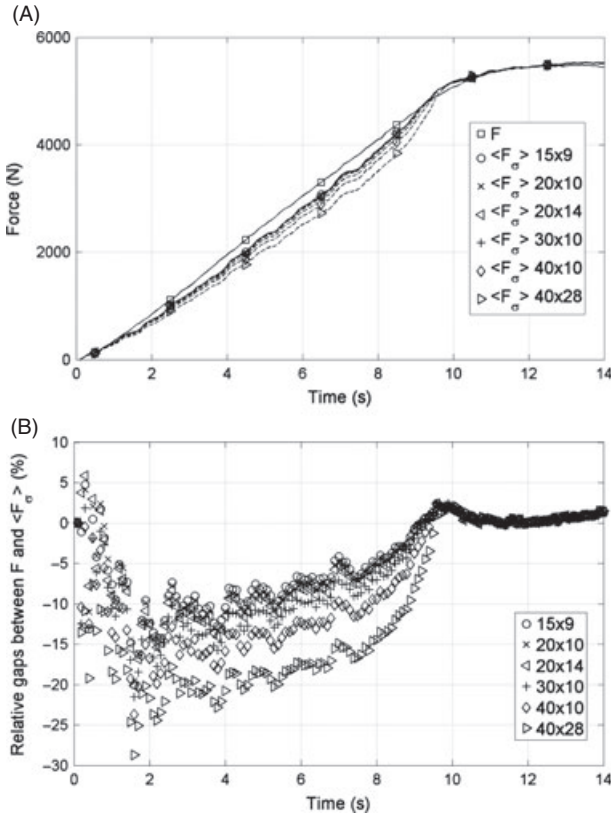

Figure 22: Influence of digital image correlation's spatial parameters on computed forces for quasi-static loading of specimen *R*12 – (A) force time histories; (B) relative gaps between F and $<F_\sigma>$

Conclusion

This article investigates the identification of the whole set of parameters of Johnson–Cook's viscoplastic model using the VFM. Strain fields are measured by DIC on flat notched specimens subjected to tensile loadings. The VFM allows the whole characterisation of JC's viscoplastic model by performing only two tests, by taking advantage of its ability to deal with heterogeneous mechanical fields. First, a test performed under quasi-static loading conditions allows the characterisation of the plastic (i.e. rate-independent) part of the model; then, dynamic loading conditions allow the characterisation with the VFM of the material strain-rate sensitivity with only one dynamic test. In comparison, costly classical procedures of identification need to perform several tests, at constant strain-rate.

The results demonstrate the ability of the VFM to characterise strongly nonlinear constitutive laws as the identification of plastic parameters is precise and robust. Moreover, the VFM is able to identify the value of the

doi: 10.1111/str.12010

viscoplastic parameter, *M*, that best describes the strain-rate sensitivity of a material, for any given value of the viscoplastic threshold, as frequently done in classical procedures of characterisation. But above all, the method is able to identify the couple of viscoplastic parameters that best describe the strain-rate sensitivity, without needing any subjective analysis of the user. In addition, the method can be used to predict the behaviour of a material when low and high strain-rates develop simultaneously in the specimen tested. It is worth noting that the ability of the VFM to address heterogeneous strain and strain-rate fields makes it possible to handle high local values of strain-rate, with no need to perform tests at high displacement rates using hydraulic jack or split Hopkinson devices.

Further developments of the VFM can be expected in the near future. The most important improvements concern the computation of the internal virtual work. Errors of computation of mechanical fields by the return-mapping algorithm are proven to be limited. On the contrary, the process of the VFM (as all methods that handle full-fields measurements) is logically strongly affected by improper field measurements by DIC. In particular, the issue of spatial resolution is a key point. For example, a too low density of points of measurement can affect the value of the ROI's surface and consequently that of the internal virtual work. Nevertheless, results are proven to be easily improved by using a corrective factor for the loss of total surface. Trickier is the issue of biased values of measured strain fields, because of large size of facets, for example, that is why, as when processing any other method of identification, the user must ensure the highest quality of measurement it is possible to achieve.

Recently, tests of characterisation of damage behaviour models using the VFM with numerically simulated strain fields have lead to satisfying results. A short-term perspective is therefore to identify damage parameters and also failure criteria using the VFM with experimental strain fields' measurements, using DIC techniques. Last, a possible improvement of the VFM could concern the development of advanced virtual fields to limit the sensitivity of results to noisy data.

ACKNOWLEDGEMENTS

The authors are grateful to the European Union, the *Région Nord-Pas-de-Calais*, the CISIT research program (http://www.cisit.org), and the French Ministry of Defence and Ministry of Research for their financial support of the DRSC Laboratory (Collisions and Rapid Structural Dynamics) with the participation of ONERA/DADS/CRD, UVHC/LAMIH and CNRS. The authors wish to especially thank Pr. F. Pierron for his very valuable critical comments which significantly contributed to this paper. Last, the authors are grateful to Dr. B. Bourel and Mr. E. Deletombe for their valuable remarks improving the drafting of this article.

REFERENCES

1. Coruk, E. and Karadoğan, C. (2011) Flow curve evaluation by optic strain measurements and force balance at the most critical section in the neck region of a tensile specimen. In: *Steel Research International, Special Edition*. *ICTP* 2012 (10th International Conference on Technology of Plasticity, Aachen, Germany, 25–30 September 2011), ed. Gerhard Hirt, A. Erman Tekkaya, Wiley-VCH Verlag GmbH & Co. KGaA. Weinheim, ISSN: 1611-3683, ISBN: 978-3-514-00784-0, September 2011..
2. Lauro, F., Bennani, B., Morin, D. and Epee, A. F. (2010) The SEE method for determination of behaviour laws for strain rate dependent material: application to polymer material. *Int. J. Impact Eng.* **37**, 715–722.
3. Chu, T. C., Ranson, W. F., Sutton, M. A., and Petters, W. H. (1985) Application of digital image correlation techniques to experimental mechanics. *Exp. Mech.* **3**, 232–244.
4. Sutton, M. A., Wolters, W. J., Perters, W. H., Ranson, W. F. and McNeill, S. R. (1983) Determination of displacements using an improved digital image correlation method. *Image Vis. Comput.* **1**, 133–139.
5. Sutton, M. A., McNeill, S. R., Helm, J. and Chao, Y. J. (2000) Advances in two-dimensional and three-dimensional computer vision. *Proc. Photomecanics, Topics Appl. Phys.* **77**, 323–372.
6. Patorski, K. (1993) *Handbook of the Moiré Fringe Technique*. Elsevier, Amsterdam.
7. Post, D., Han, B. and Ifju, P. (1994) *High Sensitivity Moiré: Experimental Analysis for Mechanics and Materials*. Springer-Verlag, New York.
8. Dainty, J. C. (1984) *Laser speckle and related phenomenon*. Springer, Berlin.
9. Parks, V. J. (1993) Geometric moiré, Chapter 6. In: *Handbook on Experimental Mechanics*, 2nd edn (A. S. Kobayashi, Ed.). VCH Publishers, New York: 267–296.
10. Surrell, Y. (1994) Moiré and grid methods: a signal processing approach. In: *Interferometry '94: Photomechanics* (Ryszard J. Pryputniewicz and Jacek Stupnicki, Eds.). Proc. SPIE Vol. 2342, p. 118–127.
11. Surrell, Y. (2005) La technique de la grille et ses applications. *Instrum. Mes. Métrol.* **4**, 193–216.
12. Avril, S., Bonnet, M. and Bretelle, A. S. *et al.* (2008) Overview of identification methods of mechanical parameters based on full-field measurements. *Exp. Mech.* **48**, 381–402.
13. Cottin, N., Felgenhauer, H. P. and Natke, H. G. (1984) On the parameter identification of elastomechanical systems using input and output residuals. *Ing. Arch.* **54**, 378–387.
14. Hemez, F. M. and Farhat, C. (1993) Updating finite element dynamic models using element-by-element sensitivity methodology. *AIAA J.* **31**, 1702–1711.
15. Meuwissen, M. H. H., Oomens, C. W. J., Baaijens, F. P. T., Petterson, R. and Janssen, J. D. (1998) Determination of the elasto-plastic properties of aluminium using a mixed numerical-experimental method. *J. Mater. Process. Technol.* **75**, 204–211.
16. Markiewicz, E., Ducrocq, P. and Drazetic, P. (1998) An inverse approach to determine the constitutive model parameters from axial crushing of thin-walled square tubes. *Int. J. Impact Eng.* **21**, 433–449.
17. Symonds, P. S. (1967) *Survey of Methods of Analysis for Plastic Deformation of Structures Under Dynamic Loading*. Technical Report; BU/NSRDC, No 1–67, 1967; Division of Engineering, Brown University, Providence, RI, USA.
18. Kajberg, J., Sundin, K. G., Melin, L. G. and Stahle, P. (2004) High strain-rate tensile testing and viscoplastic parameter identification using microscopic high-speed photography. *Int. J. Plast.* **20**, 561–575.

doi: 10.1111/str.12010

19. Perzyna, P. (1963) The constitutive equations for rate-sensitive plastic materials. *J. Appl. Math.* **20**, 321–332.
20. Kajberg, J. and Wikman, B. (2007) Viscoplastic parameter estimation by high strain-rate experiments and inverse modelling – Speckle measurements and high-speed photography. *Int. J. Solids Struct.* **44**, 145–164.
21. Johnson, G. R. and Cook, W. H. (1983) *A Constitutive Model and Data for Metals Subjected to Large Strains, High Strain Rates and High Temperatures*. Proceeding of the 7th International Symposium on Ballistics, The Hague, The Netherlands: 541–547.
22. Coppieters, S., Cooreman, S., Sol, H., Van Houtte, P. and Debruyne, D. (2011) Identification of the post-necking hardening behaviour of sheet metal by comparison of the internal and external work in the necking zone. *J. Mater. Process. Technol.* **211**, 545–552.
23. Claire, D., Hild, F. and Roux, S. (2004) A finite element formulation to identify damage fields. *Int. J. Numer. Methods Eng.* **61**, 189–208.
24. Ikehata, M. (1990) Inversion formulas for the linearized problem for an inverse boundary value problem in elastic prospection. *SIAM J. Appl. Math.* **50**, 1635–1644.
25. Grédiac, M. (1989) Principe des travaux virtuels et identification. *C. R. Acad. Sci. II Paris* **309**, 1–5.
26. Grédiac, M., Pierron, F. and Surrel, Y. (1999) Novel procedure for complete in-plane composite characterization using a T-shaped specimen. *Exp. Mech.* **39**, 142–149.
27. Grédiac, M. and Vautrin, A. (1990) A new method for determination of bending rigidities of thin anisotropic plates. *J. Appl. Mech.*. **57**, 964–968.
28. Grédiac, M., Fournier, N., Paris, P. A. and Surrel, Y. (1998) Direct identification of elastic constants of anisotropic plates by modal analysis: experiments and results. *J. Sound Vib.* **210**, 645–659.
29. Grédiac, M., Toussaint, E. and Pierron, F. (2002a) Special virtual fields for the direct determination of material parameters with the virtual fields method. 1–Principle and definitions. *Int. J. Solids Struct.* **39**, 2691–2705.
30. Grédiac, M., Toussaint, E. and Pierron, F. (2002b) Special virtual fields for the direct determination of material parameters with the virtual fields method. 2–Application to in-plane properties. *Int. J. Solids Struct.* **39**, 2707–2730.
31. Grédiac, M., Toussaint, E. and Pierron, F. (2003) Special virtual fields for the direct determination of material parameters with the virtual fields method. 3–Application to the bending rigidities of anisotropic plates. *Int. J. Solids Struct.* **40**, 2401–2419.
32. Avril, S., Grédiac, M. and Pierron, F. (2004) Sensitivity of the virtual fields method to noisy data. *Comput. Mech.* **34**, 439–452.
33. Toussaint, E., Grédiac, M. and Pierron, F. (2006) The virtual fields method with piecewise virtual fields. *Int. J. Mech. Sci.* **48**, 256–264.
34. Avril, S., Pierron, F., Pannier, Y. and Rotinat, R. (2008b) Stress reconstruction and constitutive parameter identification in plane-stress elasto-plastic problems using surface measurements of deformation fields. *Exp. Mech.* **48**, 403–419.
35. Blanchard, S., Langrand, B., Fabis, J. and Markiewicz, E. (2008) *Identification of plastic behaviour parameters from strongly heterogeneous strain field*. Proceeding of the SEM XIth International Congress and Exposition on Experimental and Applied Mechanics, Orlando, FL.
36. Grédiac, M. and Pierron, F. (2006) Applying the virtual fields method to the identification of elasto-plastic constitutive parameters. *Int. J. Plast.* **22**, 602–627.
37. Pierron, F., Avril, S. and The Tran, V. (2010) Extension of the virtual fields method to elasto-plastic material identification with cyclic loads and kinematic hardening. *Int. J. Solids Struct.* **47**, 2993–3010.
38. Rossi, M. and Pierron, F. (2012) Identification of plastic constitutive parameters at large deformations from three dimensional displacement fields. *Comput. Mech.* **49**, 53–71.
39. Giraudeau, A. and Pierron, F. (2005) Identification of stiffness and damping properties of thin isotropic vibrating plates using the virtual fields method: theory and simulations. *J. Sound Vib.* **284**, 757–781.
40. Giraudeau, A., Pierron, F. and Guo, B. (2010) An alternative to modal analysis for material stiffness and damping identification from vibrating plates. *J. Sound Vib.* **329**, 1653–1672.
41. Moulart, R., Pierron, F., Hallett, S. R. and Wisnom, M. R. (2011) Full-field strain measurement and identification of composites moduli at high strain rate with the virtual fields method. *Exp. Mech.* **51**, 509–536.
42. Pierron, F. and Forquin, P. (2011) *Ultra High Speed Full-Field Strain Measurements on Spalling Tests on Concrete Materials*. Proceedings of Annual SEM Conference, Mohegan Sun, Uncasville, CT.
43. Avril, S., Pierron, F., Sutton, M. A. and Yan, J. (2008c) Identification of elasto-visco-plastic parameters and characterization of Lüders behavior using digital image correlation and the virtual fields method. *Mech. Mater.* **40**, 729–742.
44. Notta, D., Langrand, B., Markiewicz, E. and Bourel, B. (2011) *An Advanced Procedure to Identify Viscoplastic Parameters Using the Virtual Fields Method*. International Symposium on Plasticity, Plasticity 2011, 3–8 January 2011. Puerto Vallarta: Mexico.
45. Lee, W. S. and Lin, C. F. (1998) Plastic deformation and fracture behaviour of Ti-6Al-4V alloy loaded with high strain rate under various temperatures. *Mater. Sci. Eng.* **A241**, 48–59.
46. Meyer, H. W. and Kleponis, D. S. (2001) Modeling the high strain rate behavior of titanium undergoing ballistic impact and penetration. *Int. J. Impact Eng.* **26**, 509–521.
47. Peirs, J., Verleysen, P., Van Paepegem, W. and Degrieck, J. (2011) Determining the stress-strain behaviour at large strains from high strain rate tensile and shear experiments. *Int. J. Impact Eng.* **38**, 406–415.
48. Langrand, B., Geoffroy, P., Petiniot, J. L., Fabis, J., Markiewicz, E. and Drazetic, P. (1999) Identification technique of constitutive model parameters for crashworthiness modelling. *Aerosp. Sci. Technol.* **4**, 215–227.
49. Johnson, G. R. (1985) Strength and fracture characteristics of a Titanium alloy (.06Al,.04V) subjected to various strains, strain rates, temperatures and pressures. In: Technical Report; NSWC TR, 1985; Naval Surface Weapons Center, Dahlgren, VA, 86–144.
50. Ducrocq, P., Markiewicz, E., Harmand, S., De Luca, P. and Drazetic, P. (1998) Thermal influence on mild steel behaviour during a crash event. *Int. J. Crashworth.* **3**, 163–190.
51. Haugou, G., Markiewicz, E., Fabis, J. and Gary, G. (2004) Contribution to the definition of a partial overlapping plastic strain rates domain for moderate loadings – Application to tensile testing on metallic materials. *Int. J. Crashworth.* **9**, 187–194.
52. Haugou, G., Markiewicz, E. and Fabis, J. (2006) On the use of the non-direct tensile loading on a classical split Hopkinson bar apparatus dedicated to sheet metal specimen characterisation. *Int. J. Impact Eng.* **32**, 778–798.
53. Germain, P. (1986) Mécanique X – École Polytechnique. *Ellipses* **1**, 82–102.
54. Lagarias, J. C., Reeds, J. A., Wright, M. H. and Wright, P. E. (1998) Convergence properties of the Nelder–Mead Simplex method in low dimensions. *SIAM J. Optim.* **9**, 112–147.
55. Hansen, N. and Ostermeier, A. (2001) Completely derandomized self-adaptation in evolution strategies. *Evol. Comput.* **9**, 159–195.

56. Hansen, N. and Kern, S. (2004) Evaluating the CMA Evolution Strategy on multimodal test functions. In: *Parallel Problem Solving from Nature – PPSN VIII*. Lecture Notes in Computer Science (X. Yao, E. K. Burke, J. A. Lozano, J. Smith, J. J. Merelo-Guervós, J. A. Bullinaria, J. E. Rowe, P. Tino, A. Kabán and H-P. Schwefel, Eds). Springer, Berlin, Heidelberg: 282–291.
57. Wu, T., Coret, M. and Combescure, A. (2011) Strain localisation and damage measurement by full 3D digital image correlation: application to 15-5PH stainless steel. *Strain* **47**, 49–61.
58. Haddadi, H. and Belhabib, S. (2008) Use of rigid-body motion for the investigation and estimation of the measurement errors related to digital image correlation technique. *Opt. Lasers Eng.* **46**, 185–196.
59. Fazzini, M., Mistou, S., Dalverny, O. and Robert, L. (2010) Study of image characteristics on digital image correlation error assessment. *Opt. Lasers Eng.* **48**, 335–339.
60. Boyer, R., Welsch, G. and Collings, E. W. (1994) *Materials Properties Handbook: Titanium Alloys*. ASM International, Materials Park, OH.
61. Simo, J. C. and Hughes, T. J. R. (1998) *Computational Inelasticity, Vol. 7 Interdisciplinary Applied Mechanics*. Springer, Berlin.
62. Pierron, F., Sutton, M. A. and Tiwari, V. (2011) Ultra high speed DIC and Virtual Fields Method analysis of a three point bending impact test on an aluminium bar. *Exp. Mech.* **51**, 509–536.

APPENDIX A: CLASSICAL PROCEDURE OF CHARACTERISATION OF THE JC'S MODEL

This appendix describes how the mechanical quantities, measured as described in Johnson–Cook's Viscoplastic Behaviour Model, for example, are analysed in the classical procedure of characterisation of the JC's viscoplastic model of behaviour.

First, true stress, σ, and strain, ε, are analysed from measured nominal stress, σ_n, and strain, ε_n, using the following relations:

$$\varepsilon = \ln(1+\varepsilon_n) \text{ and } \sigma = \sigma_n(1+\varepsilon_n)$$

with $\sigma_n = F/S_0$ obtained from force time histories and initial cross section of the specimen; $\varepsilon_n = \Delta L/L_0$ is the uniaxial relative elongation. The Young modulus, E, is given by the slope of the linear part of the true stress versus true strain diagram. In our case, no strain-rate effect was observed and a value of 114 *GP*a was identified for E. Note that the Poisson coefficient, ν, was not measured but a bibliographic value of 0.342 [60] was considered. Elastic strain, ε^e, is computed following Hooke's law for an isotropic one-dimensional behaviour, i.e. $\varepsilon^e = \frac{\sigma}{E}$. Plastic strain, ε^p, is obtained assuming strain partition, i.e. $\varepsilon^p = \varepsilon - \varepsilon^e$. Raw experimental true stress versus plastic strain diagrams are then plotted at several strain-rates (Figure 23). In our case, values of $\dot{\varepsilon}^p$ were assumed to be the average of the derivative of total strain time history measured during each dynamic test. Values of 5, 41, 265 and 469 s^{-1} were obtained for displacement rates of 0.1, 1, 6 and 10 m s^{-1}, respectively. It is interesting to note that the jack could not maintain a constant strain-rate at the displacement rate of 1 m s^{-1} (mean value of $\dot{\varepsilon}^p$ equals to 41 s^{-1}). This explains the oscillations of the corresponding stress versus plastic strain diagram (Figure 23) and gives an illustration of the difficulty to perform tests at constant strain-rate, particularly under dynamic loading conditions. Finally, one should note that the maximum plastic strain was about 5% before necking (i.e. $d\sigma/d\varepsilon = 0$).

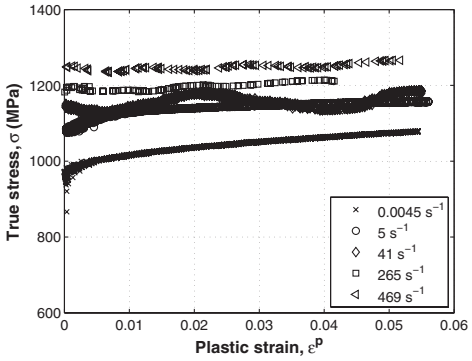

Figure 23: Classical procedure for viscoplastic behaviour characterisation: true stress *versus* plastic strain diagrams

The parameters of JC's model are identified in two steps. First, results obtained at low strain-rate (i.e. displacement rate of 2 mm min^{-1} here) are analysed to characterise the rate-independent part of the hardening law, governed by parameters σ_0, K and n. Conventionally, the initial yield stress, σ_0, is the true stress reached for $\varepsilon^p = 0.2\%$. This value was closed to 973 MPa. Isotropic hardening parameters, K and n, are those that lead to the best correlation between the quasi-static experimental results, until necking appears, and the model, according to the logarithmic expression (23) of the rate-independent part of isotropic hardening law. This way, the linear regression equation $y = 0.5632x + 6.3231$ gave the values of 557.3 MPa and 0.5632 for K and n, respectively, with the coefficient of determination, R^2 equals to 0.9874 (Figure 24). Note that the coefficient of determination is actually the square of the correlation coefficient. Obviously, the closer the value of R^2 is to one, the better the linear regression fits the data.

$$\ln(\sigma - \sigma_0) = \ln K + n \ln \varepsilon^p \tag{23}$$

In the second step, results at higher strain-rates are used to identify the viscoplastic parameters $\dot{\varepsilon}_0$ and M. The isotropic hardening law in viscoplasticity, Equation (2), is rewritten in the following form:

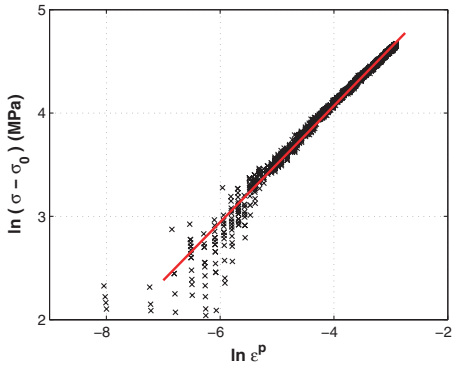

Figure 24: Linear regression to characterise the plastic part of Johnson–Cook's model

doi: 10.1111/str.12010

$$\left(\frac{\sigma(\varepsilon^p,\dot{\varepsilon}^p)}{\sigma_0+K(\varepsilon^p)^n}-1\right)=M(\ln(\dot{\varepsilon}^p)-\ln(\dot{\varepsilon}_0))$$

In our case, results of dynamic loadings were plotted for the four levels of estimated strain-rate. It is worth noting that gaps between data and the model were more important than in quasi-static conditions (Figure 25A). In addition to a more important dispersion of data, these gaps also came from possible variations of the strain-rate during tests (whereas it was assumed to stay constant), as already pointed out for the test at estimated strain-rate of 41 s^{-1}. An additional challenge to identify the strain rate sensitivity following the JC's model is the lack of uniqueness of the couple of viscoplastic parameters (this point is discussed more deeply in the main parts of this article). It explains why it is common to set the viscoplastic threshold to an arbitrarily fixed value (generally 1 s^{-1}) and to identify parameter M only, when performing classical procedures of identification [46, 49]. Otherwise, it is possible to look for both viscoplastic parameters simultaneously but performing the linear regression to identify parameters M and $\dot{\varepsilon}_0$ is not easy (Figure 25B). In our case, values of 0.0151 and 1.16 10^{-2} s^{-1} were found out for M and $\dot{\varepsilon}_0$, respectively, with a quite poor coefficient of determination, $R^2 = 0.4431$, when the linear regression was built taking into account all dynamic results. A better value of $R^2 = 0.7447$ was obtained when considering data at $\dot{\varepsilon}^p$ equal to 5, 265 and 469 s^{-1}, with an identified value of 5.37 10^{-2} s^{-1} for $\dot{\varepsilon}_0$ and 0.0209 for M. Finally, a linear regression using results obtained for the three highest strain-rates gave values of 1.29 s^{-1} and 0.0329 for $\dot{\varepsilon}_0$ and M, respectively ($R^2 = 0.4943$). An objective criterion would have been to select parameters' values associated to the higher coefficient of determination. Nevertheless, a viscoplastic threshold of 5.37 10^{-2} s^{-1} was judged too low compared to commonly encountered values (close or equal to 1 s^{-1}) and was rejected. Note that such a low threshold value would have raised the issue of the modelling of viscous effects during tests (performed under loading conditions commonly considered as quasi-static, i.e. rate independent. Finally, values of 1.29 s^{-1} and 0.0329 for $\dot{\varepsilon}_0$ and M, respectively, were selected as the best compromise.

The values of JC's material parameters for the Ti6Al4V identified using this usual procedure are summarised in Table 1 Johnson–Cook's Viscoplastic Behaviour Model section.

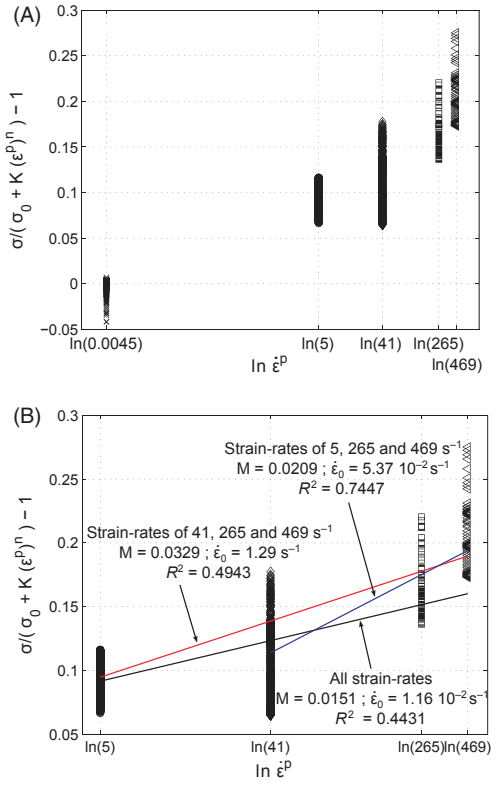

Figure 25: Exploitation of dynamic tests to identify viscoplastic parameters – (A) scattering of data; (B) linear regressions on dynamic results

APPENDIX B: RETURN-MAPPING ALGORITHM

A return-mapping algorithm is implemented to compute mechanical quantities from measured strain fields, following the constitutive equations of the Johnson–Cook's model of behaviour (cf. Johnson–Cook's Viscoplastic Behaviour Model). Its scheme is an adaptation of work of Simo and Hughes's for J_2-plasticity [61]. Mechanical quantities at time step $k + 1$ are computed from measured total strains at instant t_{k+1} and computed mechanical quantities at previous time step k, using an implicit Euler scheme for temporal integration. An elastic state is assumed at t_0 to initialise the algorithm. With an implicit scheme (unconditionally stable), the time step, and consequently the experimental frame rate of strain measurement, are unconstrained. Moreoever, it was demonstrated that the use of an implicit scheme improves the stability of computations.

The total strain tensor, $\bar{\varepsilon}$, is divided into an elastic (reversible) part, $\bar{\varepsilon}^e$, and a viscoplastic part, $\bar{\varepsilon}^{vp}$, such that $\bar{\varepsilon} = \bar{\varepsilon}^e + \bar{\varepsilon}^{vp}$. In the current work, no kinematic hardening is taken into account and the temperature softening is neglected. It leads to the expressions (24) and (25) for the JC's isotropic hardening law and for the yield surface, f, respectively. Last, a plane stress state is assumed. One can note that the plane stress hypothesis is required because of surface measurements of strain fields, although the VFM can deal with three-dimensional fields.

$$\sigma_y=\underbrace{(\sigma_0+Kp^n)}_{\sigma_y^p}\left(1+M\ln\left(\frac{\dot{\varepsilon}_{eq}^{vp}}{\dot{\varepsilon}_0}\right)\right) \tag{24}$$

$$f=J_2(\bar{\sigma})-\sigma_y\le 0 \tag{25}$$

with notations of Johnson–Cook's Viscoplastic Behaviour Model. It is reminded that $J_2(\bar{\sigma})$ is actually the von Mises equivalent stress.

In the hardening law (24), the rate-independent part, σ_y^p, is approximated by a piecewise linear function of cumulated plastic strain, p, for each interval $[p_i;p_{i+1}[$, so that:

$$\sigma_y^p(p)=\sigma_y^p(p_i)+K'(p-p_i)\ \forall p\in[p_i;p_{i+1}[\tag{26}$$

$\sigma_y^p(p_i)$ is the actual values of the rate-independent part of

the yield stress computed at $p = p_i$, that is, $\sigma_y^p(p_i) = \sigma_0 + Kp_i^n \ \forall i$. K' is the slope of the piecewise linear law, that is, $K' = \frac{\sigma_y^p(p_{i+1}) - \sigma_y^p(p_i)}{p_{i+1} - p_i} = K\frac{p_{i+1}^n - p_i^n}{p_{i+1} - p_i}$. In practice, $p_0 = 0$ and $p_{i+1} = p_i + 10^{-4} \ \forall i$. To simplify the notations, variables α and $\sigma_0{}'$ are respectively defined by $\alpha = p - p_i$ and $\sigma_0' = \sigma_y^p(p_i)$.

In the framework of associated (visco-)plasticity, an expression of the plastic multiplier, γ, is:

$$\frac{\partial \bar{\varepsilon}^{vp}}{\partial t} = \dot{\gamma}\frac{\partial f}{\partial \bar{\sigma}} \tag{27}$$

It comes from the expression (25) of f that $\frac{\partial \bar{\varepsilon}^{vp}}{\partial t} = \dot{\gamma}\sqrt{\frac{3}{2}}\frac{\bar{S}}{J_2(\bar{\sigma})}$, with $\bar{S}$ the deviatoric part of $\bar{\sigma}$. The time derivative operator is expressed in its usual discretised form, i.e. $\frac{\partial x}{\partial t}\big|_{k+1} = \frac{\Delta x}{\Delta t}$ ($\frac{\partial \bar{x}}{\partial t}\big|_{k+1} = \frac{\Delta \bar{x}}{\Delta t}$, respectively) with x ($\bar{x}$) any scalar or tensor, respectively, and $\Delta x = x_{k+1} - x_k$ ($\Delta x_{ij} = x_{ij,k+1} - x_{ij,k}$) its increment between instants t_{k+1} and t_k ($\Delta t = t_{k+1} - t_k$). The discretisation of the expression (27) therefore leads to the expressions (28) and (29) for the increments of viscoplastic strain and of cumulated viscoplastic strain, respectively.

$$\Delta \bar{\varepsilon}^{vp} = \sqrt{\frac{3}{2}}\Delta\gamma\frac{\bar{S}_{k+1}}{J_2(\bar{\sigma}_{k+1})} \tag{28}$$

$$\Delta p = \sqrt{\frac{2}{3}\Delta\bar{\varepsilon}^{vp} : \Delta\bar{\varepsilon}^{vp}} = \Delta\gamma\frac{\sqrt{\bar{S}_{k+1} : \bar{S}_{k+1}}}{J_2(\bar{\sigma}_{k+1})} = \sqrt{\frac{2}{3}}\Delta\gamma \tag{29}$$

The scheme of the algorithm is divided in two steps. First, a purely elastic evolution is assumed between increments k and $k + 1$, corresponding to instants t_k and t_{k+1} of strain measurement, respectively. The general expression of the Hooke's linear elastic laws for an isotropic material (30) is used to define the elastic trial step, see Equation (31).

$$\bar{\sigma} = 2\mu\bar{\varepsilon}^e + \lambda tr(\varepsilon^e)\bar{I} \tag{30}$$

with μ and λ the Lamé coefficients. *tr* stands for the trace operator and $\bar{I}$ is the 3×3 identity matrix.

$$\left|\begin{array}{l}
\bar{\varepsilon}^{e,\text{trial}} = \bar{\varepsilon}_k^e + \Delta\bar{\varepsilon} = \bar{\varepsilon}_{k+1} - \bar{\varepsilon}_k^{vp} \\
\bar{\varepsilon}^{vp,\text{trial}} = \bar{\varepsilon}_k^{vp} \text{and } p^{\text{trial}} = p_k \\
\bar{\sigma}^{\text{trial}} = 2\mu\left(\bar{\varepsilon}_{k+1} - \bar{\varepsilon}_k^{vp}\right) + \lambda\left[tr(\bar{\varepsilon}_{k+1}) - \underbrace{tr\left(\bar{\varepsilon}_k^{vp}\right)}_{=0}\right] \\
\dot{\varepsilon}_{eq}^{vp,\text{trial}} = \dfrac{J_2\left(\bar{\sigma}^{\text{trial}}\right) - J_2(\bar{\sigma}_k)}{3\mu\Delta t} \\
\text{if } \dot{\varepsilon}_{eq}^{vp,\text{trial}} > \dot{\varepsilon}_0 \\
\quad f^{\text{trial}} = J_2\left(\bar{\sigma}^{\text{trial}}\right) - \left(\sigma_{0,k}' + K_k'\alpha_k\right)\left(1 + M\ln\left(\dfrac{\dot{\varepsilon}_{eq}^{\text{trial}}}{\dot{\varepsilon}_0}\right)\right) \\
\text{else} \\
\quad f^{\text{trial}} = J_2\left(\bar{\sigma}^{\text{trial}}\right) - \left(\sigma_{0,k}' + K_k'\alpha_k\right)
\end{array}\right. \tag{31}$$

If $f^{\text{trial}} < 0$, mechanical quantities at increment $k + 1$ are updated considering an elastic evolution, i.e. in particular $\bar{\sigma}_{k+1} = \bar{\sigma}^{\text{trial}}$, $\bar{\varepsilon}_{k+1}^{vp} = \bar{\varepsilon}_k^{vp}$ and $p_{k+1} = p_k$. Otherwise, a plastic correction is needed. In the current implementation, it is based on a loop computation of the plastic multiplier, γ (27). First, the actual yield surface at increment $k + 1$ is expressed using approximation (26):

$$f_{k+1} = J_2(\bar{\sigma}_{k+1}) - \left(\sigma_{0,k+1}' + K_{k+1}'\alpha_{k+1}\right)\left(1 + M\ln\left(\frac{\dot{\varepsilon}_{eq,k+1}^{vp}}{\dot{\varepsilon}_0}\right)\right) = 0 \tag{32}$$

with $\alpha_{k+1} = p_{k+1} - p_i$. Since p_{k+1} is unknown, the value of p_k is used to find out p_i, i.e. $p_k \in [p_i; p_{i+1}[$. Consequently, $K_{k+1}' = K_k' = \frac{p_{i+1}^n - p_i^n}{p_{i+1} - p_i}$ (both noted K'), $\sigma_{0,k+1}' = \sigma_{0,k}' = \sigma_0 + Kp_i^n$ (both noted σ_0') and $\Delta p = \Delta\alpha$. Its expression is obtained by combining the expressions of f^{trial} (31) and f_{k+1} (32):

$$\begin{aligned}
\Delta p &= \alpha_{k+1} - \alpha_k \\
&= \frac{J_2(\bar{\sigma}_{k+1}) - \sigma_0'(1 + A_{k+1})}{K'(1 + A_{k+1})} - \frac{J_2\left(\bar{\sigma}^{\text{trial}}\right) - f^{\text{trial}} - \sigma_0'(1 + A_k)}{K'(1 + A_k)} \\
&= \frac{J_2(\bar{\sigma}_{k+1})(1 + A_k) - J_2\left(\bar{\sigma}^{\text{trial}}\right)(1 + A_{k+1}) + f^{\text{trial}}(1 + A_{k+1})}{K'(1 + A_k)(1 + A_{k+1})}
\end{aligned} \tag{33}$$

with $A_k = M\ln\left(\frac{\dot{\varepsilon}_{eq,k}^{vp}}{\dot{\varepsilon}_0}\right)$ and $A_{k+1} = M\ln\left(\frac{\dot{\varepsilon}_{eq,k+1}^{vp}}{\dot{\varepsilon}_0}\right)$.

From the definition (31) of $\bar{\sigma}^{\text{trial}}$ it comes immediately that $\bar{\sigma}^{\text{trial}} = \bar{\sigma}_{k+1} + 2\mu\Delta\bar{\varepsilon}^{vp}$ and therefore $\bar{S}^{\text{trial}} = \bar{S}_{k+1} + 2\mu\Delta\bar{\varepsilon}^{vp}$, since $tr(\Delta\bar{\varepsilon}^{vp}) = 0$ (hypothesis of plastic incompressibility). Then, using the relation (28), $\bar{S}^{\text{trial}} = (1 + 2\mu\sqrt{\frac{3}{2}}\frac{\Delta\gamma}{J_2(\bar{\sigma}_{k+1})})\bar{S}_{k+1}$. Finally, $J_2\left(\bar{\sigma}^{\text{trial}}\right) = J_2(\bar{\sigma}_{k+1}) + 2\mu\sqrt{\frac{3}{2}}\Delta\gamma$. Combining this relation with relations (33) and (29) gives the expression (34) for the plastic multiplier. One can already note that $\frac{\bar{S}^{\text{trial}}}{J_2(\bar{\sigma}^{\text{trial}})} = \frac{\bar{S}_{k+1}}{J_2(\bar{\sigma}_{k+1})}$.

$$\Delta\gamma = \frac{J_2(\bar{\sigma}_{k+1})(A_k - A_{k+1}) + f^{\text{trial}}(1 + A_{k+1})}{\left[\sqrt{\frac{2}{3}}K'(1 + A_k) + 2\mu\right](1 + A_{k+1})} \tag{34}$$

The value of $\Delta\gamma$ is computed using a loop (cf. Table 9), initialised with $A_{k+1} = A_k$ and $J_2(\bar{\sigma}_{k+1}) = J_2\left(\bar{\sigma}^{\text{trial}}\right)$. $A_k = 0$ if $\dot{\varepsilon}_{eq,n}^{vp} \leq \dot{\varepsilon}_0$. The final value of $\Delta\gamma$ is reached after $N = 50$ iterations (arbitray value, in practice, about 20 iterations are actually needed to ensure convergence). Mechanical quantities are then updated using relations (35). Finally, the expression of the yield surface is updated by computing new values of K' and σ'_0. The admissibility of stress states as well as the respect of the plane-stress state are verified. The Table 9 gives the complete scheme of the algorithm.

$$\left|\begin{array}{l}
\Delta\bar{\varepsilon}^{vp} = \sqrt{\dfrac{3}{2}}\Delta\gamma\dfrac{\bar{S}_{k+1}}{J_2(\bar{\sigma}_{k+1})} = \sqrt{\dfrac{3}{2}}\Delta\gamma\dfrac{\bar{S}^{\text{trial}}}{J_2(\bar{\sigma}^{\text{trial}})} \\
\bar{\varepsilon}_{k+1}^{vp} = \bar{\varepsilon}_k^{vp} + \Delta\bar{\varepsilon}^{vp} \\
\bar{\varepsilon}_{k+1}^{e} = \bar{\varepsilon}_{k+1} - \bar{\varepsilon}_{k+1}^{vp} \\
p_{k+1} = p_k + \sqrt{\dfrac{2}{3}}\Delta\gamma \\
\dot{\varepsilon}_{eq,k+1}^{vp} = \dfrac{3}{2}\dfrac{\Delta p}{\Delta t} \\
\bar{\sigma}_{k+1} = \bar{\sigma}^{\text{trial}} - 2\mu\Delta\bar{\varepsilon}^{vp}
\end{array}\right. \tag{35}$$

doi: 10.1111/str.12010

Table 9: Return-mapping algorithm for viscoplastic model of Johnson–Cook

Inputs: $\bar{\varepsilon}_{k+1}$, variables at increment k, material parameters.
Outputs: variables at increment $k+1$.

Computation of σ'_0, K' and $\alpha_k = p_k - p_i$
Computation of elastic trial step: $\bar{\sigma}^{trial}$, $J_2\left(\bar{\sigma}^{trial}\right)$, $\dot{\varepsilon}_{eq}^{vp,trial}$ (31)
If $\dot{\varepsilon}_{eq}^{vp,trial} \leq \dot{\varepsilon}_0$**, then:**
$f^{trial} = J_2\left(\bar{\sigma}^{trial}\right) - \left(\sigma'_0 + K'\alpha_k\right)$
Else:
$f^{trial} = J_2\left(\bar{\sigma}^{trial}\right) - \left(\sigma'_0 + K'\alpha_k\right)\left(1 + M\ln\left(\frac{\dot{\varepsilon}_{eq}^{vp,trial}}{\dot{\varepsilon}_0}\right)\right)$
End.
If $f^{trial} > 0$**, then:**
If $\dot{\varepsilon}_{eq}^{vp,trial} \leq \dot{\varepsilon}_0$**, then:**
$\Delta\gamma = \frac{f^{trial}}{\sqrt{\frac{2}{3}}K' + 2\mu}$
Else:
$\Delta\gamma = \frac{f^{trial}}{\sqrt{\frac{2}{3}}K'\left(1 + M\ln\left(\frac{\dot{\varepsilon}_{eq,k}^{vp}}{\dot{\varepsilon}_0}\right)\right) + 2\mu}$
End.
For $i = 1$ **to** N**, do:**
$p_{k+1} = p_k + \sqrt{\frac{2}{3}}\Delta\gamma$
$\dot{\varepsilon}_{eq,k+1}^{vp} = \frac{3}{2}\frac{p_{k+1} - p_k}{\Delta t}$
$J_2\left(\bar{\sigma}_{k+1}\right) = J_2\left(\bar{\sigma}^{trial}\right) - 2\mu\sqrt{\frac{3}{2}}\Delta\gamma$
If $\dot{\varepsilon}_{eq,k+1}^{vp} > \dot{\varepsilon}_0$**, then:**
If $\dot{\varepsilon}_{eq,k}^{vp} > \dot{\varepsilon}_0$**, then:**
$\Delta\gamma = \frac{J_2(\bar{\sigma}_{k+1})M\left[\ln\left(\frac{\dot{\varepsilon}_{eq,k}^{vp}}{\dot{\varepsilon}_0}\right) - \ln\left(\frac{\dot{\varepsilon}_{eq,k+1}^{vp}}{\dot{\varepsilon}_0}\right)\right] + f^{trial}\left[1 + M\ln\left(\frac{\dot{\varepsilon}_{eq,k+1}^{vp}}{\dot{\varepsilon}_0}\right)\right]}{\left[\sqrt{\frac{2}{3}}K'\left(1 + M\ln\left(\frac{\dot{\varepsilon}_{eq,k}^{vp}}{\dot{\varepsilon}_0}\right)\right) + 2\mu\right]\left[1 + M\ln\left(\frac{\dot{\varepsilon}_{eq,k+1}^{vp}}{\dot{\varepsilon}_0}\right)\right]}$
Else:
$\Delta\gamma = \frac{-J_2(\bar{\sigma}_{k+1})M\ln\left(\frac{\dot{\varepsilon}_{eq,k+1}^{vp}}{\dot{\varepsilon}_0}\right) + f^{trial}\left[1 + M\ln\left(\frac{\dot{\varepsilon}_{eq,k+1}^{vp}}{\dot{\varepsilon}_0}\right)\right]}{\left[\sqrt{\frac{2}{3}}K' + 2\mu\right]\left[1 + M\ln\left(\frac{\dot{\varepsilon}_{eq,k+1}^{vp}}{\dot{\varepsilon}_0}\right)\right]}$
End.
Else:
$\Delta\gamma = \frac{f^{trial}}{\sqrt{\frac{2}{3}}K' + 2\mu}$
End.
End.
Update of mechanical quantities:
$\Delta\bar{\varepsilon}^{vp} = \sqrt{\frac{3}{2}}\Delta\gamma\frac{\bar{S}^{trial}}{J_2\left(\bar{\sigma}^{trial}\right)}$
$\bar{\varepsilon}_{k+1}^{vp} = \bar{\varepsilon}_k^{vp} + \Delta\bar{\varepsilon}^{vp}$
$\bar{\varepsilon}_{k+1}^{e} = \bar{\varepsilon}_{k+1} - \bar{\varepsilon}_{k+1}^{vp}$
$p_{k+1} = p_k + \sqrt{\frac{2}{3}}\Delta\gamma$
$\dot{\varepsilon}_{eq,k+1}^{vp} = \frac{3}{2}\frac{\Delta p}{\Delta t}$
$\bar{\sigma}_{k+1} = \bar{\sigma}^{trial} - 2\mu\Delta\bar{\varepsilon}^{vp}$
Update of the hardening law's rate-independent part: $p_{k+1} \in [p_j; p_{j+1}[$
Computation of σ'_0, K' and $\alpha_{k+1} = p_{k+1} - p_j$
Update of the yield surface:
If $\dot{\varepsilon}_{eq,k+1}^{vp} > \dot{\varepsilon}_0$**, then:**
$f_{k+1} = J_2\left(\bar{\sigma}_{k+1}\right) - \left(\sigma'_0 + K'\alpha_{k+1}\right)\left(1 + M\ln\left(\frac{\dot{\varepsilon}_{eq,k+1}^{vp}}{\dot{\varepsilon}_0}\right)\right)$
Else:
$f_{k+1} = J_2\left(\bar{\sigma}_{k+1}\right) - \left(\sigma'_0 + K'\alpha_{k+1}\right)$
End.
Test of admissibility of stress states:
If $f_{k+1} \neq 0$, then: correction of $\bar{\sigma}_{k+1}$
Else:
Elastic evolution: updated quantities at increment $n+1$ are equal to trial test quantities.
End.
Computation of through-thickness strain (plane-stress hypothesis).

doi: 10.1111/str.12010